Article

Sensitive multicolor indicators for monitoring norepinephrine in vivo

 Check for updates

Zacharoula Kagiampaki [1,8], Valentin Rohner [1,8], Cedric Kiss [1,8],
Sebastiano Curreli [2], Alexander Dieter [3,4], Maria Wilhelm[1],
Masaya Harada [1], Sian N. Duss [5], Jan Dernic[1], Musadiq A. Bhat [1],
Xuehan Zhou[1], Luca Ravotto[1], Tim Ziebarth [6], Laura Moreno Wasielewski[6],
Latife Sönmez[6], Dietmar Benke[1,7], Bruno Weber [1,7], Johannes Bohacek [5,7],
Andreas Reiner [6], J. Simon Wiegert [3,4], Tommaso Fellin [2] &
Tommaso Patriarchi [1,7] ✉

Genetically encoded indicators engineered from G-protein-coupled receptors are important tools that enable high-resolution in vivo neuromodulator imaging. Here, we introduce a family of sensitive multicolor norepinephrine (NE) indicators, which includes nLightG (green) and nLightR (red). These tools report endogenous NE release in vitro, ex vivo and in vivo with improved sensitivity, ligand selectivity and kinetics, as well as a distinct pharmacological profile compared with previous state-of-the-art GRAB$_{NE}$ indicators. Using in vivo multisite fiber photometry recordings of nLightG, we could simultaneously monitor optogenetically evoked NE release in the mouse locus coeruleus and hippocampus. Two-photon imaging of nLightG revealed locomotion and reward-related NE transients in the dorsal CA1 area of the hippocampus. Thus, the sensitive NE indicators introduced here represent an important addition to the current repertoire of indicators and provide the means for a thorough investigation of the NE system.

The development of genetically encoded fluorescent indicators based on engineering of circularly permuted green fluorescent protein (cpGFP) into G-protein-coupled receptors (GPCRs), hereafter called GPCR-based indicators, permits the in vivo optical detection of neuromodulators with high spatial and/or temporal resolution[1,2]. These indicators complement previously available techniques for monitoring neuromodulators in vivo (microdialysis, fast-scan cyclic voltammetry, CniFERs, iTango)[1,2]. The addition of red indicators to this class of tools further expanded potential applications, for example by enabling their combination with blue light-excited optogenetic tools or multiplexed

imaging of neurotransmitters[3,4]. However, red indicators are so far only available for detecting dopamine (DA).

The neuromodulator NE carries out important functions in the brain, including the regulation of wakefulness, alertness and the response to stress, among others[5,6]. Despite the growing need for tools to directly probe NE in vivo their availability is currently limited, due partly to the labor-intensive screening efforts required for their development[7]. In fact, a large number of GPCR-based indicator variants (typically hundreds to thousands) needs to be screened in mammalian cells to identify candidate protein variants with suitable properties

[1]Institute of Pharmacology and Toxicology, University of Zürich, Zürich, Switzerland. [2]Optical Approaches to Brain Function Laboratory, Istituto Italiano di Tecnologia, Genoa, Italy. [3]Research Group Synaptic Wiring and Information Processing, Center for Molecular Neurobiology Hamburg, University Medical Center Hamburg-Eppendorf, Hamburg, Germany. [4]Department of Neurophysiology, MCTN, Medical Faculty Mannheim, Heidelberg University, Mannheim, Germany. [5]Institute for Neuroscience, Department of Health Sciences and Technology, ETH Zürich, Zürich, Switzerland. [6]Cellular Neurobiology, Department of Biology and Biotechnology, Ruhr University Bochum, Bochum, Germany. [7]Neuroscience Center Zurich, University and ETH Zürich, Zürich, Switzerland. [8]These authors contributed equally: Zacharoula Kagiampaki, Valentin Rohner, Cedric Kiss. ✉e-mail: patriarchi@pharma.uzh.ch

for in vivo applications[4,7–9]. Current state-of-the-art NE indicators (GRAB$_{NE}$) enable optical detection of NE in vivo, but are based solely on an Alpha-2a adrenergic receptor (AR) (Alpha-2 AR) scaffold[7]. A diversification of the currently available toolkit would thus be desirable.

Here, we developed next-generation NE indicators by using a previously unexplored receptor subtype. Adopting an Alpha-1a adrenergic receptor (Alpha-1 AR) as a scaffold, we engineered nLightG and nLightR, two sensitive green and red fluorescent NE indicators, respectively. We benchmarked these tools in multiple experimental settings and demonstrated that they exhibit a distinct pharmacological profile, as well as improved sensitivity, ligand selectivity and kinetics compared with a state-of-the-art GRAB$_{NE}$ indicator. Using these sensors, we could accurately detect endogenous NE release both ex vivo and in vivo with a variety of techniques (widefield imaging, multisite fiber photometry and two-photon microscopy). Our family of NE indicators offers ready-to-use tools for a more complete investigation of NE physiology.

Results

Development of multicolor NE indicators

Despite the large sequence diversity of GPCRs, their structures and activation mechanisms are conserved[10], and their seven transmembrane helices typically align well in space[11]. Thus, to expand the family of NE indicators we explored a grafting-based approach. Here, domains from the previously optimized green and red fluorescent DA indicators dLight1.3b[8] and RdLight1 (ref. [3]), comprising the circularly permuted fluorescent protein as well as parts of transmembrane helices V and VI were directly grafted onto target Alpha-1 ARs of choice.

Given that currently available NE indicators are green, we first tested our strategy by attempting the development of a red fluorescent NE indicator, generating five indicator prototypes based on Alpha-1 ARs from different species (house mouse, budgerigar, king cobra, zebrafish and sperm whale). The fluorescent protein module was inserted according to a sequence alignment based on the Ballesteros–Weinstein (BW) numbering scheme[12]. Of note, structural alignment of the sperm whale Alpha-1 AR (swAlpha-1 AR) with the human DA receptor D1 (hmDRD1) (Supplementary Fig. 1) also indicated structural conservation at the insertion positions chosen based on BW numbering. All five prototype indicators were detectable on the membrane of transiently transfected HEK293T cells and gave a positive fluorescence response ($\Delta F/F_0$) in the range of 100% to 180% upon addition of 10 µM NE (Extended Data Fig. 1a,b). The indicators based on the sperm whale, budgerigar and zebrafish Alpha-1 ARs showed the highest basal brightness and were selected for the determination of the EC$_{50}$ of NE and DA. Of these three indicators, the sperm whale-based indicator was selected for further development as it showed both high sensitivity and selectivity for NE (EC$_{50\,(NE)}$ = 574 nM, EC$_{50\,(DA)}$ = 21.5 µM) (Extended Data Fig. 1c,d). We then tested whether the same approach could work for the development of

green fluorescent indicators by using an equivalent fluorescent protein module from dLight1.3b. The resulting NE indicator showed a $\Delta F/F_0$ response of approximately 1000%. To check whether the selected BW registries of the two modules were optimal, we systematically varied them in a parallel fashion. While the first prototype of the green fluorescent NE indicator showed the largest dynamic range, we identified an improved grafting registry for the red fluorescent NE indicator (Extended Data Fig. 1e–g).

In previous work, we discovered that mutations in the intracellular loop 2 (ICL2) can increase the fluorescence response of GPCR-based indicators[3,8,9]. Given the close proximity of the ICL2 region to transmembrane helices V and VI (Supplementary Fig. 1), we reasoned that also ICL2 grafting should be tested in the modular approach for engineering GPCR-based indicators. We grafted a module containing parts of helices III and IV and the entire ICL2 from dLight1.3b or RdLight1 onto the corresponding NE indicator prototypes. This led to an improvement in the fluorescent response for the red indicator, but not for the green indicator. Importantly, grafting the ICL2 substantially improved the selectivity for NE versus DA in both indicators (Extended Data Fig. 1h–k).

In vitro characterization of nLightG and nLightR

We next focused on characterizing the in vitro properties of our green and red fluorescent NE indicators (named nLightG and nLightR, respectively) (Fig. 1a). Both indicators localized well to the cell membrane and exhibited a similarly large fluorescence response upon stimulation with 10 µM NE in HEK293T cells and rat cortical neurons ($\Delta F/F_{0\,HEK293T}$ = 1,083 ± 47%, $\Delta F/F_{0\,neurons}$ = 671 ± 21% for nLightG; $\Delta F/F_{0\,HEK293T}$ = 158 ± 4%, $\Delta F/F_{0\,neurons}$ = 113 ± 13% for nLightR; mean ± s.e.m.; Fig. 1b–d). The activation of both indicators was fully reversed upon application of a small molecule Alpha-1 AR antagonist (trazodone (Trz); Fig. 1c,d), in contrast to the GRAB$_{NE1m}$ indicator, which was not affected by Trz but was instead fully inactivated by the Alpha-2 AR antagonist yohimbine (Yoh) (Extended Data Fig. 2a), highlighting the distinct pharmacological profiles of the two indicator classes. Furthermore, a direct comparison between nLightG and GRAB$_{NE1m}$ in HEK293T cells revealed that the indicators have similar basal brightness (Extended Data Fig. 2b). Spectral characterization of the indicators in HEK293T cells revealed peak one-photon excitations (λ_{ex}) at 498 nm and 566 nm and peak emissions (λ_{em}) at 516 nm and 594 nm for nLightG and nLightR, respectively (Extended Data Fig. 2b,c). nLightG was also excitable through two-photon illumination, which showed peak performance at 920 nm (Extended Data Fig. 2d). A key feature of GPCR-based fluorescent indicators is their inherent, naturally evolved molecular specificity. We tested a panel of eight neurotransmitters at a high concentration (10 µM) on nLightG and nLightR to check whether the molecular specificity of the swAlpha-1 AR is conserved despite the changes introduced during the indicator-engineering process. As expected, only NE, epinephrine and (to a much lower extent) DA induced a significant fluorescence

Fig. 1 | In vitro properties of nLightG and nLightR. a, Structural models of nLightG (left) and nLightR (right) generated using ColabFold[39]. **b**, Representative images of HEK293T cells and neurons expressing nLightG or nLightR before/after application of NE (10 µM) and corresponding pixel-wise $\Delta F/F_0$ heatmaps. White insets indicate surface expression of the indicators over white dashed lines. Scale bars, 10 µm (HEK293T), 20 µm (neurons). **c**, Left, timelapse of fluorescence of response ($\Delta F/F_0$) of nLightG in HEK293T (dark green) or neurons (light green) upon application of NE (10 µM) followed by application of Trz (10 µM). Right, quantification of maximal $\Delta F/F_0$ responses from left. Two-tailed Students t-test with Welch's correction; n = 3 independent experiments with n = 22 cells (HEK293T), n = 18 cells (neurons). ****P = 2.979 × 10^{-16} (HEK293T), ****P = 8.558 × 10^{-17} (neurons). **d**, Same as in **c** for nLightR. n = 3 independent experiments with n = 21 cells (HEK293T), n = 6 cells (neurons). ****P = 5.922 × 10^{-32} (HEK293T), ***P = 0.004 (neurons). **e**, Fluorescence dose-response curves of nLightG (left) and GRAB$_{NE1m}$ (right) for NE and DA in HEK293T cells normalized to

the maximum $\Delta F/F_0$ for NE for each indicator. Datapoints were fitted with four-parameter dose-response curves to determine EC$_{50}$ values. n = 6,5,3 wells for nLightG with NE, nLightG with DA and GRAB$_{NE}$ with NE/DA, respectively. **f**, Same as in **e** for nLightR with n = 3 wells. All data are shown as mean ± s.e.m. **g**, Representative heatmap of nLightG fluorescence response ($\Delta F/F_0$ (%)) in an outside-out membrane patch from nLightG-expressing HEK293T cells (n = 6 independent experiments). Scale bar, 50 µm. **h**, ON and OFF kinetics of nLightG (top) and GRAB$_{NE1m}$ (bottom) after ultrafast (<0.5 ms) switching of the perfusion pipette. Dots represent the average of five applications. Kinetic parameters were obtained using single-exponential fits on the average of all trials. **i**, Statistical comparison of kinetic parameters. Unpaired two-tailed Student's t-test. n = 6 and five patches for nLightG and GRAB$_{NE1m}$, respectively. ****P = 3.0 × 10^{-8} (τ_{ON}), ****P = 2.7 × 10^{-5} (τ_{OFF}). Mean ± s.d. are shown. **j**, Five consecutive NE applications on nLightG (5 µM, 1 s). Images were acquired at 100 Hz. All experiments were repeated at least three times with similar results.

response (Extended Data Fig. 2e–g). The EC$_{50}$ of NE was in a similar range for nLightG (EC$_{50\ HEK293T}$ = 755 ± 85 nM, EC$_{50\ neurons}$ = 937 ± 133 nM, mean ± s.e.m.) and nLightR (EC$_{50\ HEK293T}$ = 654 ± 47 nM, EC$_{50\ neurons}$ = 408 ± 55 nM, mean ± s.e.m.). In HEK293T cells the EC$_{50}$ of DA was

comparable between nLightG (EC$_{50}$ = 20.0 ± 7.9 μM, mean ± s.e.m.) and nLightR (EC$_{50}$ = 18.5 ± 6.7 μM, mean ± s.e.m.), and was approximately 30-fold higher than that of NE. Furthermore the maximal response to DA was only a small fraction of that induced by NE (23.0% for the nLightG
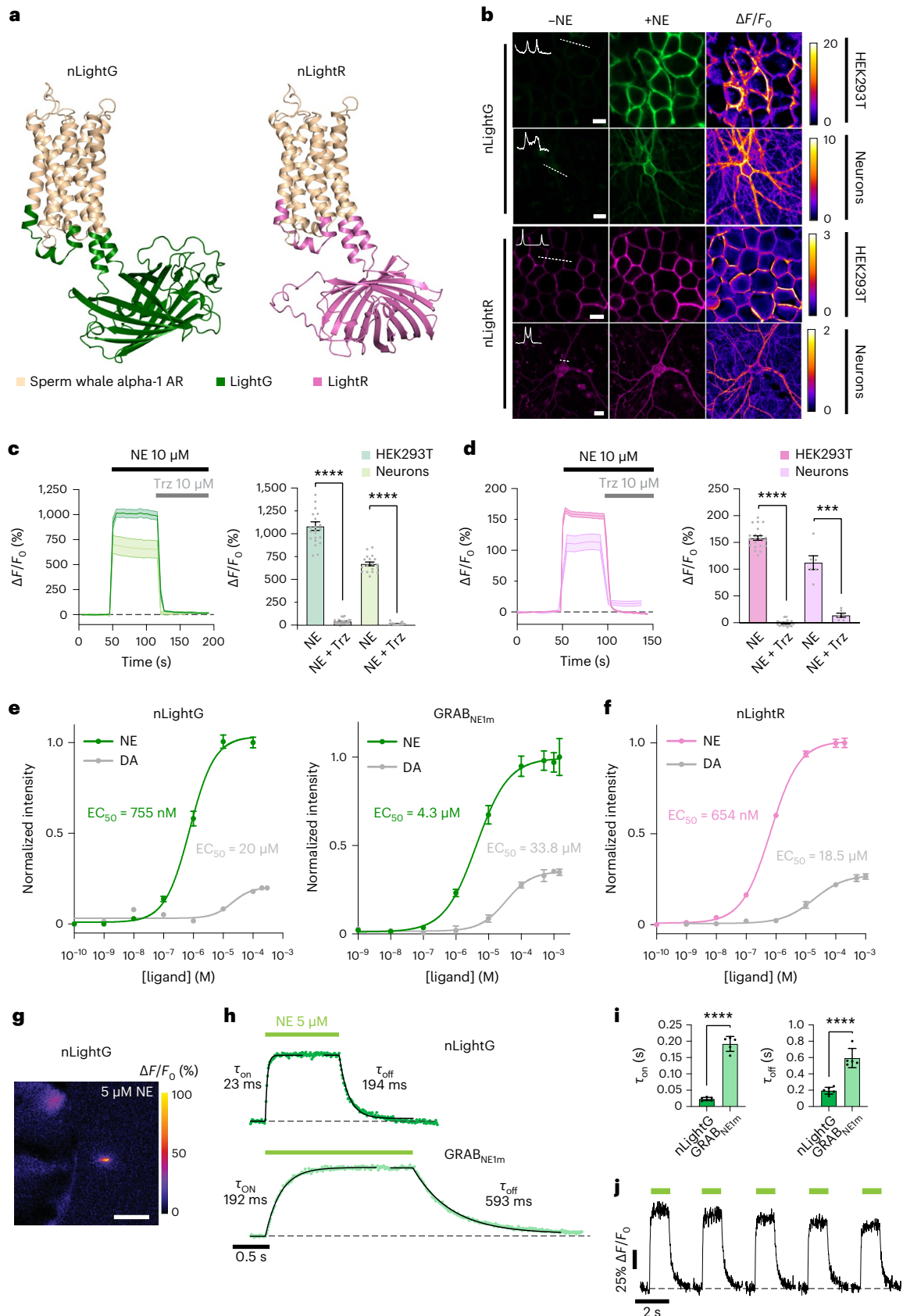
and 25.6% for nLightR), indicating that DA acts as only a partial agonist at both indicators (Fig. 1e,f). Similar measurements performed on GRAB$_{NE1m}$ revealed an EC$_{50}$ for DA, which is only eightfold higher than that for NE and that its maximal response to DA is 35% of the response to NE (Fig. 1e). These results indicate that both nLightG and nLightR have higher selectivity for NE over DA compared with GRAB$_{NE1m}$. Furthermore, in cultured neurons the maximal response of both nLightG and nLightR to DA was further reduced and amounted to less than 10% of that induced by NE (Extended Data Fig. 2e). To establish the kinetic properties and reversibility of the fluorescence response for this family of indicators, we performed patch-clamp fluorometry on outside-out membrane patches from nLightG-transfected HEK293T cells (Fig. 1g and Supplementary Video 1). Using a piezo-controlled system for rapid solution switching between 0 and 5 μM NE in less than 1 ms (ref. 13), we found that nLightG exhibited rapid activation and deactivation kinetics (τ_{on} = 23 ± 5 ms and τ_{off} = 194 ± 42 ms; mean ± s.d., six patches; Fig. 1h). Similar experiments performed on membrane patches containing GRAB$_{NE1m}$ revealed that this indicator has eightfold slower activation kinetics and threefold slower deactivation kinetics (τ_{on} = 192 ± 23 ms and τ_{off} = 593 ± 118 ms; mean ± s.d., five patches) compared with nLightG (Fig. 1h,i). These experiments also confirmed the ability of nLightG to faithfully report multiple bidirectional changes in extracellular NE concentration in rapid succession (Fig. 1j).

Intracellular signaling is the primary function of GPCRs, but should be avoided in GPCR-based fluorescent indicators. Using genetically encoded calcium indicators[14], we detected a substantial increase of intracellular Ca^{2+} concentration in response to the activation of wild-type swAlpha-1 AR with NE, confirming the coupling to Gα$_q$ pathway expected for this AR subtype[15]. In the same experimental setup, activation of nLightG and nLightR did not induce a noticeable increase in the intracellular Ca^{2+} concentration, indicating that coupling to Gα$_q$ is disrupted (Extended Data Fig. 3a–d). To further investigate the downstream coupling capabilities of nLightG, nLightR and swAlpha-1 AR, we characterized their direct interactions with mini-Gq, mini-Gs and mini-Gi[16] upon agonist stimulation using a Nanoluciferase (NanoBiT)-based complementation assay[17] (Extended Data Fig. 3e–g). Stimulation of the swAlpha-1 AR with NE showed coupling to mini-Gq and mini-Gs, but no coupling to mini-Gi. In contrast, stimulation of nLightG and nLightR with NE did not lead to coupling to mini-Gq, mini-Gs or mini-Gi. Next, we investigated whether indicator activation induces recruitment of β-arrestin-2 using the same NanoBiT-based approach. Since the Alpha-1 AR subtype has not been consistently shown to couple to β-arrestins in previous studies[18–20], we used hmDRD1 as a positive control. Stimulation with DA induced recruitment of β-arrestin-2 to DRD1, while no recruitment was observed for nLightG or nLightR upon stimulation with NE (Extended Data Fig. 3e–g). In summary, nLightG and nLightR are selective and sensitive NE indicators with minimal potential for interference with endogenous signaling pathways.

Ex vivo and in vivo benchmarking of nLightG and nLightR

We then characterized the properties of nLightG and nLightR in brain slices and benchmarked them against those of the state-of-the-art NE indicator GRAB$_{NE1m}$. To this end, adeno-associated viruses (rAAVs) carrying either nLightG, nLightR or GRAB$_{NE1m}$ driven by the human synapsin promoter were injected in the mouse lateral hypothalamus (LH) (rAAV2/9.hSynapsin1.nLightG/nLightR/GRAB$_{NE1m}$). After at least 4 weeks of expression, we prepared acute brain slices and imaged them under epifluorescence illumination (Fig. 2a). Perfusion of a high concentration of NE (50 μM) on the slices led to fluorescence responses from both nLightG and nLightR, which were reversible upon NE washout (Fig. 2b,c). Next, we compared catecholamine-selectivity and response to an Alpha-1 AR antagonist among all three NE indicators. Perfusion of a high concentration of DA (50 μM) elicited small, but detectable, fluorescence responses from nLightG and nLightR, which amounted to about 12% and 3% of the responses to an identical concentration of NE, respectively (Fig. 2d–f). In comparison, the response to the same concentration of DA for GRAB$_{NE1m}$ was larger and corresponded to about 19% of the response to NE. Furthermore, application of the Alpha-1 AR antagonist Trz (10 μM) largely reversed the NE-induced response from nLightG and nLightR while it had no effect on GRAB$_{NE1m}$, confirming that the two indicator families maintain distinct pharmacological profiles in brain tissue (Fig. 2d–f). Next, we investigated whether both nLightG and nLightR could be sensitive enough to detect endogenous NE release evoked by electrical pulses, as compared with GRAB$_{NE1m}$. We applied an increasing number of pulses to the slices (1, 10, 100 pulses) and quantified evoked fluorescence responses (Fig. 2g). Stimulus-evoked responses could be detected for both nLightG and GRAB$_{NE1m}$ after application of a single pulse, while increasing the number of pulses was mirrored by a parallel increase in the responses (Fig. 2h,i). Fluorescence responses could also be detected from nLightR-expressing slices upon application of 10 or 100 pulses, but not to a single pulse (Fig. 2j), indicating that also the red NE indicator can detect endogenous NE release.

Alpha-2 ARs are densely expressed presynaptically and on the somata of locus coeruleus (LC) NE-producing neurons[21,22], where they provide feedback inhibition in response to NE release. Accordingly, Alpha-2 AR antagonists, such as Yoh, are known to increase natural LC excitability in response to external stimuli[23], resulting in increased NE release[24]. Due to their intrinsic sensitivity to Alpha-2 AR-targeting drugs, Alpha-2 AR-based NE indicators (that is, the GRAB$_{NE1}$ family[7]) cannot be utilized to faithfully monitor the effects of these drugs on endogenous NE release. To determine whether nLightG and nLightR could overcome this limitation due to their orthogonal receptor pharmacology, we performed a side-by-side comparison in vivo with GRAB$_{NE1m}$ using fiber photometry during systemic administration of subtype-selective AR antagonists. To reliably monitor NE release, we adopted a previously established tail-lifting assay[7] (Fig. 2k). Mice received injections of saline (Sal), Trz (1 mg kg^{-1}) or Yoh (4 mg kg^{-1}) in separate trials followed by five consecutive tail-lifting events (Fig. 2l). Tail-lifting of the animals

Fig. 2 | Ex vivo and in vivo benchmarking of nLightG and nLightR.
a, Experiment schematics. **b**, Left, representative nLightG response to perfusion of NE (50 μM) and washout. Right, quantification of nLightG responses (two-sided paired t-test, *P = 0.0308, n = 4 slices from three mice). **c**, Same as **b** for nLightR (two-sided paired t-test, *P = 0.0434, n = 4 slices from two mice). **d**, Left, representative nLightG response to subsequent perfusions of DA (50 μM), NE (50 μM) and Trz (10 μM). Right, quantification of nLightG responses (repeated measures one-way ANOVA, P = 0.0006 and Tukey's multiple comparison test, ***P = 0.0005 for DA against NE and **P = 0.0087 for NE against NE + Trz, n = 6 slices from two mice). **e**, Same as **d** for nLightR (repeated measures one-way ANOVA, P = 0.0040 and Tukey's multiple comparison test, **P = 0.0034 for DA against NE and **P = 0.0277 for NE against NE + Trz, n = 4 slices from two mice). **f**, Same as **e** for GRAB$_{NE1m}$ (repeated measures one-way ANOVA, P = 4.572 × 10^{-5} and Tukey's multiple comparison test, ****P = 8.501 × 10^{-5} for DA against NE, n = 7 slices from three mice). NS, not significant. **g**, Representative images of indicator expression and fluorescence responses. Scale bars, 100 μm. **h**, Left, average traces of nLightG responses to electrical stimulation using increasing numbers of pulses (1, 10, 100 pulses). Right, quantification of peak responses (two-tailed paired t-test, **P = 0.0018, n = 9 slices from two mice). **i**, Same as in **h** for GRAB$_{NE1m}$; n = 8 slices from three mice. **j**, Same as in **i** for nLightR; n = 6 slices from two mice. **k**, Schematics of experimental procedures. **l**, Timeline of experiments. **m**, Left, average traces of fluorescence response from nLightG-expressing animals after injection of different drugs. Right, quantification of peak ΔF/F$_0$ responses from left. Peak values were compared with the control (Sal). **P = 0.0013 for Trz, *P = 0.0345 for Yoh, n = 8 mice. **n**, Same as **m** for GRAB$_{NE1m}$. P = 0.9010 for Trz (NS), **P = 0.0015 for Yoh, n = 7 mice. **o**, Same as **m**, for nLightR. *P = 0.0329 for Trz, P = 0.457 for Yoh (NS), n = 5 mice. **m–o**, Blue shades indicate tail-lifting period. Analyses were performed with repeated measures one-way ANOVA with Dunnett's multiple comparisons test. **b–o**, All data are mean ± s.e.m. All experiments were repeated at least three times with similar results.

caused a stable and reproducible increase in nLightG signal (mean peak $\Delta F/F_0$ = 8.7%), which lasted for the entire duration of the event (Fig. 2m). Similar signals, although with smaller amplitudes, were

detected in GRAB$_{NE1m}$ (mean peak $\Delta F/F_0$ = 4.8%) and nLightR-expressing animals (mean peak $\Delta F/F_0$ = 2.6%) (Fig. 2n,o). Administration of Trz reduced the tail-lift-induced response of nLightG and nLightR,
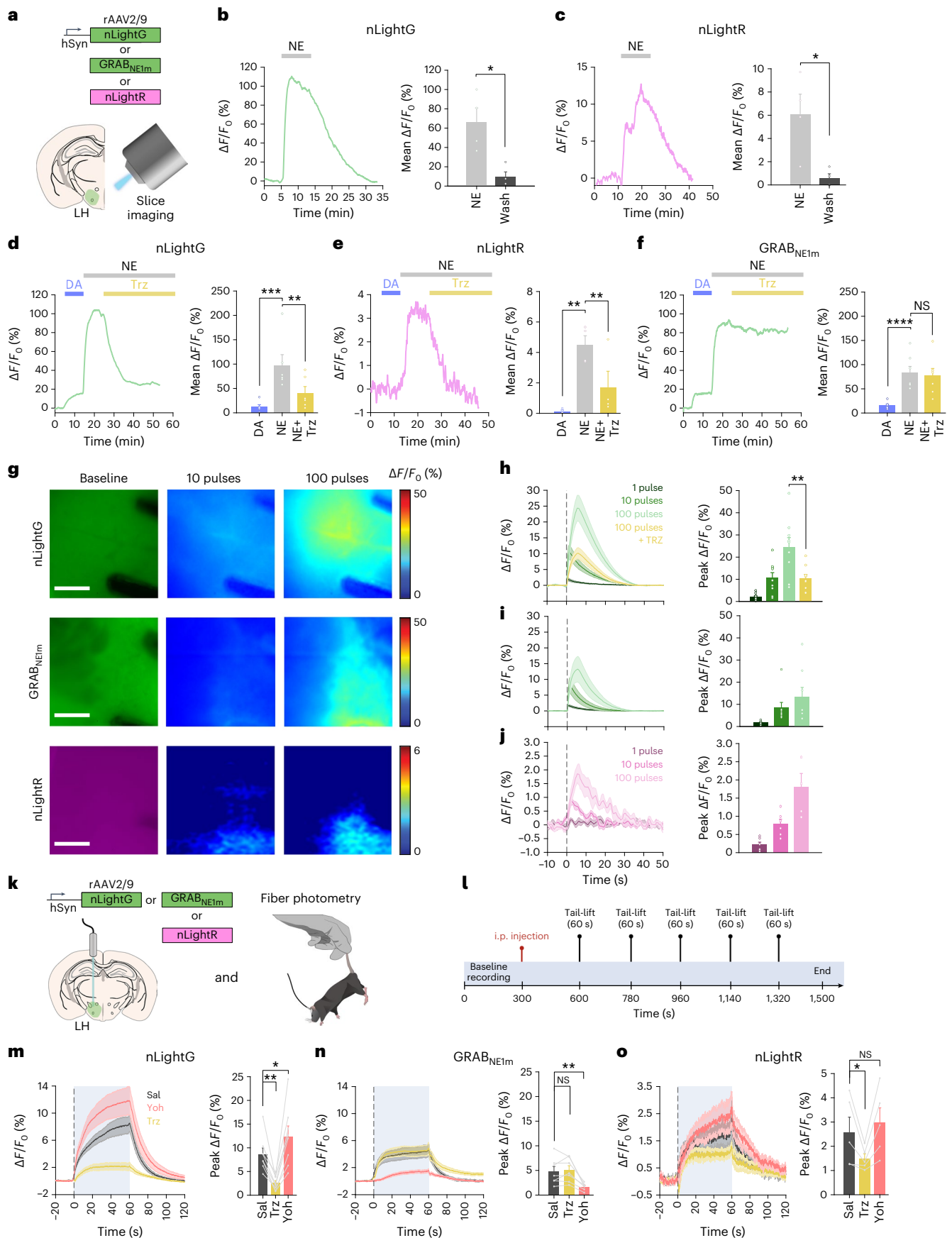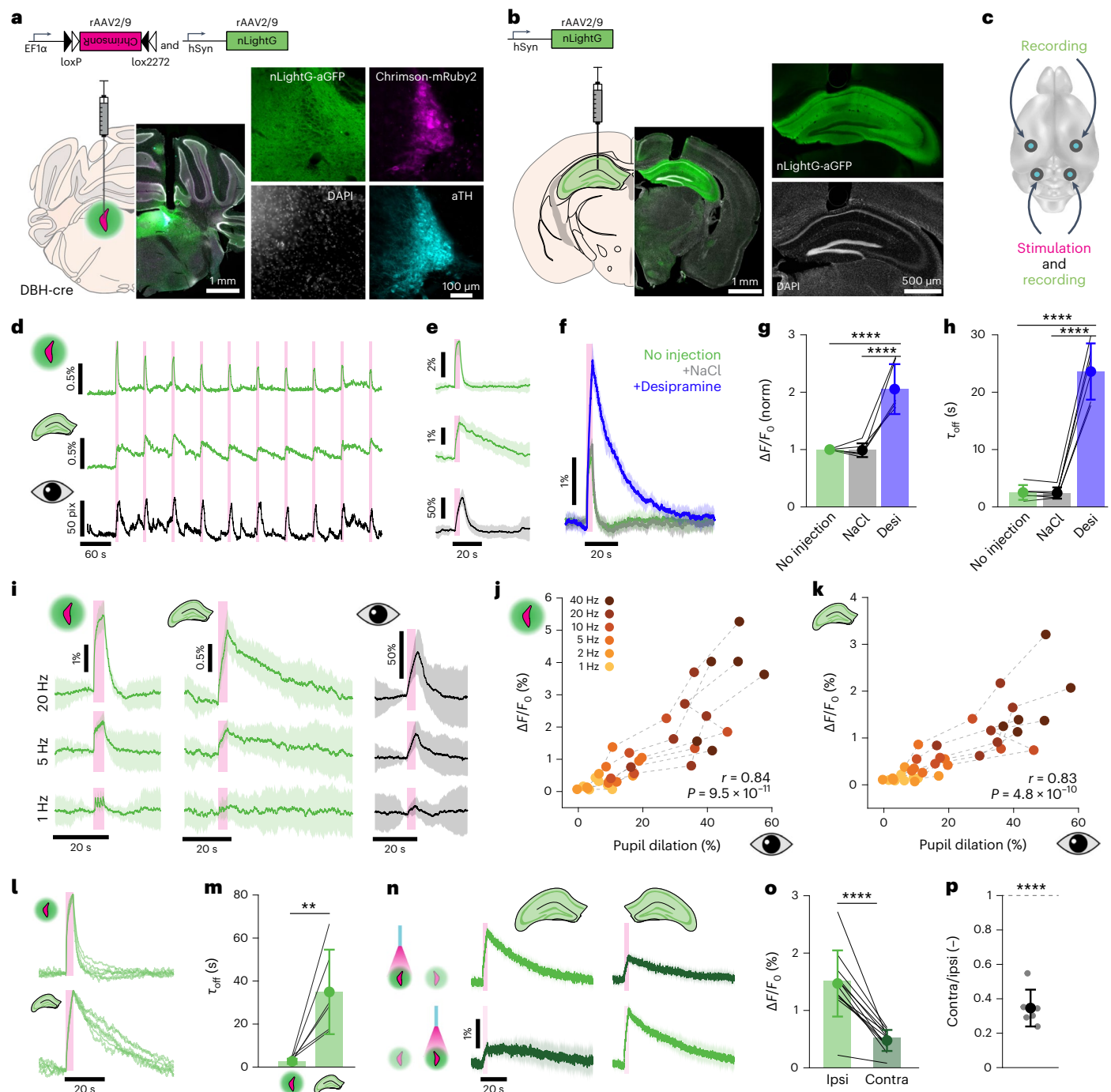
Fig. 3 | In vivo dual-site recording of optogenetically evoked NE release using nLightG. a–c, Experimental schematics (**c**) and histological verification for targeting LC (**a**) and dHPC (**b**). **d**, Example traces of pupil diameter (bottom) and simultaneously recorded nLightG fluorescence in the dHPC (center) and LC (top) upon optogenetic LC stimulation (4-s-long pulse train with 20 ms pulses at 40 Hz; 595 nm; 10 mW at fiber tip; pink bars). **e**, Mean ± s.d. of the recording shown in **d** ($n = 20$ trials). **f**, Mean ± s.d. of nLightG fluorescence from LC in response to optogenetic stimulation ($n = 15$ trials, one mouse) performed after indicated treatments. **g**, Peak $\Delta F/F_0$ of baseline-normalized averaged responses (one-way ANOVA, $P = 3.17 \times 10^{-6}$ and Tukey's test, ****$P = 1 \times 10^{-4}$/****$P = 1 \times 10^{-5}$ for no injection/NaCl versus desipramine (Desi); $n = 6$ mice). **h**, τ_{off} of averaged responses (one-way ANOVA, $P = 1.89 \times 10^{-9}$ and Tukey's test, ****$P = 9.8 \times 10^{-9}$/****$P = 9.4 \times 10^{-9}$ for no injection/NaCl versus desipramine; $n = 6$ mice) shown in **f**. **i**, Mean ± s.d. of simultaneously recorded nLightG fluorescence in the LC (left), dHPC (center), as well as pupil diameter (right) in an exemplary mouse, in response to pulses presented at 1, 5 and 20 Hz ($n = 20$ trials each).

j,**k**, Peak $\Delta F/F_0$ of averaged nLightG fluorescence in the LC (**j**) and dHPC (**k**) as a function of pupil dilation upon optogenetic stimulation (Pearson's correlation coefficient $r = 0.84/0.83$, $P = 9.5 \times 10^{-11}/4.8 \times 10^{-10}$ for LC/dHPC; $n = 6$ mice). **l**, Normalized responses of simultaneously recorded nLightG in the LC (top) and dHPC (bottom), during optogenetic LC stimulation ($n = 6$ mice). **m**, τ_{off} of averaged responses shown in **l**. **$P_{10} = 0.0025$, two-sided two-sample t-test, $n = 6$ mice. **n**, Mean ± s.d. of simultaneously recorded nLightG fluorescence from hippocampi in both hemispheres (columns) upon stimulation of either the left (top) or the right (bottom) LC ($n = 15$ trials each). **o**, Peak $\Delta F/F_0$ of each dHPC upon ipsilateral (Ipsi, left) or contralateral (Contra, right) LC stimulation. ****$P_{11} = 1.97 \times 10^{-7}$, two-sided one-sample t-test, $n = 12$ dHPC from $n = 6$ mice. **p**, Contralateral divided by ipsilateral average response per mouse; 34.6 ± 11%; ****$P_5 = 2.4 \times 10^{-5}$, two-sided one-sample t-test against 1 (indicated by dashed line); $n = 6$ mice. **n**, **o** and **p** were recorded under isoflurane anesthesia, all others in awake mice. All data are shown as mean ± s.d.

while it had no effect on GRAB$_{NE1m}$ signals. Conversely, Yoh administration increased tail-lift induced responses from nLightG and nLightR, in line with the known disinhibitory effect of this drug on the LC system. In the case of GRAB$_{NE1m}$, Yoh administration strongly attenuated the indicator response, an effect that had been reported previously[7] (Fig. 2m–o). Finally, to determine whether the NE release-promoting effect was mediated by Yoh via the Alpha-2 AR feedback loop, hence requiring conscious LC modulation by external stimuli, we also tested the effect of this drug on optogenetically driven NE release in the ventral hippocampus (vHPC) during anesthesia (Extended Data Fig. 4a,b). Under these conditions, Yoh attenuated optogenetically evoked NE signals monitored via GRAB$_{NE1m}$, while it did not have an effect on the NE signals reported by nLightG (Extended Data Fig. 4c,d). Overall, these results confirm that nLightG and nLightR have a pharmacological profile distinct to the GRAB$_{NE1m}$ family indicators, which offers a valuable option to monitor the effects of Alpha-2 AR-targeting drugs on the endogenous NE system in vivo.

Optogenetic dissection of NE release across brain areas

We next asked whether we could use the most sensitive of our NE indicators (nLightG) for detecting optogenetically evoked NE release simultaneously in two brain areas with fiber photometry (Extended Data Fig. 5). We bilaterally injected rAAV2/9.hSynapsin1.nLightG in the dorsal hippocampus (dHPC) and rAAV2/9.hSynapsin1.DIO. ChrimsonR-mRuby2 together with rAAV2/9.hSynapsin1.nLightG in the LC of DBH-cre mice (Fig. 3a–c). Optogenetic stimulation of the LC using 595 nm light (4 s pulse train, 20 ms pulses at 40 Hz, 10 mW at fiber tip), led to NE signals that occurred simultaneously in both LC and dHPC. As a second readout of LC activation, we measured pupil diameter[25], which, as expected, increased rapidly upon each optical stimulus (Fig. 3d,e). To establish the contribution of NE reuptake mechanisms on nLightG signals in the LC, we repeated the recordings after intraperitoneal (i.p.) injections of Sal or the NE transporter (NET) blocker desipramine. Sal injection did not alter the nLightG response profile, while desipramine led to an increase in both the magnitude and decay kinetics of the response (Fig. 3f–h), confirming the dependence of the nLightG response on extracellular NE. We then investigated the effects of different stimulation frequencies of optogenetic LC activation on nLightG responses in LC and dHPC and on pupil dilation. In the LC, nLightG responses could be detected at stimulation frequencies as low as 1 Hz (Fig. 3i). Upon increasing the frequency of optical stimuli, we found a strong, positive linear correlation between nLightG responses and pupil dilation in both recorded brain areas (Fig. 3j,k). The decay kinetics of nLightG responses to the same frequency of stimulation (40 Hz) were slower in the dHPC (τ_{off} = 37.3 ± 21 s, mean ± s.d.) compared with the LC (τ_{off} = 2.8 ± 1.3 s, mean ± s.d.) (Fig. 3l,m), presumably reflecting differences in the density or functionality of local NE reuptake mechanisms. Finally, we used nLightG to explore the lateralization of noradrenergic innervation of the dHPC[26,27]:

we found that unilateral LC stimulation most efficiently drove NE release in the ipsilateral dHPC, and that ipsilateral optogenetically evoked dHPC-nLightG signals were approximately threefold larger than the contralateral ones (Fig. 3n–p).

Two-photon imaging of NE release in the dHPC

Next, we tested whether nLightG could be used in combination with two-photon excitation to image NE release in vivo with high spatial resolution. We expressed nLightG in the CA1 region of the hippocampus and imaged nLightG signals through a chronic optical window using two-photon microscopy in awake head-fixed mice navigating in a virtual corridor (n = 4 mice; Fig. 4a,b). Mice received a water reward positioned along the corridor and the same field-of-view (FOV) was imaged in five sessions on five consecutive days (one session for each imaging day; Fig. 4c,d).

Since previous reports[28,29] show that LC-projections activity is higher during locomotion and reward delivery, we tested the hypothesis that nLightG signals correlate positively with locomotion and reward. We first computed event-triggered averages of nLightG signals over the whole FOV based on the time at which the mouse started to run (magenta color in Fig. 4e–g). While nLightG signal remained similar to baseline after the initial start of running on day 1 of recording, we found that, after the mouse started to run, nLightG signals increased with respect to baseline in the following days (days 2–5; Fig. 4e and Extended Data Fig. 6a). Running speed dynamics were comparable across all five recording days. In days 2–5 (but not in day 1), the amplitude of nLightG signals correlated positively with the running speed of the animal (Fig. 4h and Extended Data Fig. 6b,c). Moreover, we investigated whether the nLightG signals that we recorded could be due to motion artifacts. We computed the structural similarity, a parameter evaluating the perceived change in structural information between individual frames with respect to the average projection of the whole imaging temporal series. We found structural similarity to be constant in the time window associated with the changes in nLightG signals described above (Extended Data Fig. 6d–f). Moreover, we performed temporal shuffling of nLightG traces and found that the shuffling procedure destroyed the positive deflection of nLightG signals that we observed when traces were not shuffled (dashed horizontal line in Extended Data Fig. 6a).

We then built event-triggered averages of nLightG signals over the whole FOV based on the time at which the mouse crossed the reward position (green color in Fig. 4e–g). We observed that nLightG signals showed a transient increase with respect to baseline followed by a decrease in all recording days (Fig. 4e and Extended Data Fig. 7a–c). In all five recording days, lick rate increased after the mouse crossed the reward position (Fig. 4g), while running speed decreased with respect to baseline after the mouse crossed the reward position (Fig. 4f). The amplitude of nLightG signals increased with lick rate (Fig. 4i) across all recording days, and correlated positively with running speed across

Fig. 4 | Two-photon imaging of NE signals in awake behaving mice using nLightG. a, Experiment schematics. **b**, Viral injection schematics. **c**, On days 1, 2 and 3, rewards were delivered at 85 cm from the start of the corridor. On day 3, at half of the recording session the reward delivery was repositioned to 145 cm, where it remained through days 4 and 5. **d**, Representative average time-projections of FOV (images are scaled to their maximum, scale bars 50 μm). **e**, Event-triggered averages showing changes in nLightG signal amplitude over the whole FOV upon running (magenta) and reward position crossing (green) for the 5 days of recording. **f,g**, Event-triggered averages of the speed (**f**) and normalized (norm.) lick rate (**g**) of the animals in the virtual corridor upon running initiation (magenta) and at reward position crossing (green). **h,i**, nLightG signal amplitude over the whole FOV as a function of running speed (**h**) and lick rate (**i**) for event-triggered averages upon running initiation (magenta) and reward position crossing (green, days 1–5). In **h** and **i**, *P < 0.05 two-sided rank-sum test; H0, slope of the linear model equals to 0 (for each test n = 4 animals); NS, not significant. In **h**, P values are as follows: day 1, P(run) = 2.48 ×10⁻¹, P(reward) = 2.48 ×10⁻¹;

day 2, P(run) = 2.09 × 10⁻², P(reward) = 2.48 × 10⁻¹; day 3, P(run) = 2.09 × 10⁻², P(reward) = 2.09 × 10⁻²; day 4, P(run) = 2.09 × 10⁻², P(reward) = 2.09 × 10⁻²; day 5, P(run) = 2.09 × 10⁻², P(reward) = 2.09 × 10⁻². In **i**, P value equals 2.09 × 10⁻² for all sessions. In **e–i**, lines and shaded areas indicate mean ± s.d. **j**, Representative FOV showing nLightG-expressing hippocampal CA1 neurons. White boxes indicate ROIs identified in the FOV using CITE-On[30] (scale bar, 50 μm). **k**, Event-triggered averages showing ΔF/F₀ of nLightG signal when the mouse started running for all the ROIs identified in **j**. **l**, Lower-left triangle, cross-correlation matrix for all traces extracted from the ROIs displayed in **j–k**. Upper-right triangle, corresponding hierarchical clustering. **m,n**, Same as in **k** and **l**, but for event-triggered averages when the mouse crossed the reward position. **o**, Density map showing Pearson's correlation (corr.) value of nLightG signals from pairs of ROIs during reward position crossing as a function of that obtained during running (separated by a white dashed line). Data from 897,000 pairs from 6,000 ROIs in four mice over five imaging sessions.

recording days 3–5 (Fig. 4h). We observed a structural similarity in the time window associated with the changes in nLightG signals (Extended Data Fig. 7d–f), and temporal shuffling of nLightG traces with respect to the timing in which the mouse crossed the reward position eliminated the changes of nLightG signals that we observed when traces were not shuffled (dashed horizontal line in Extended Data Fig. 7).
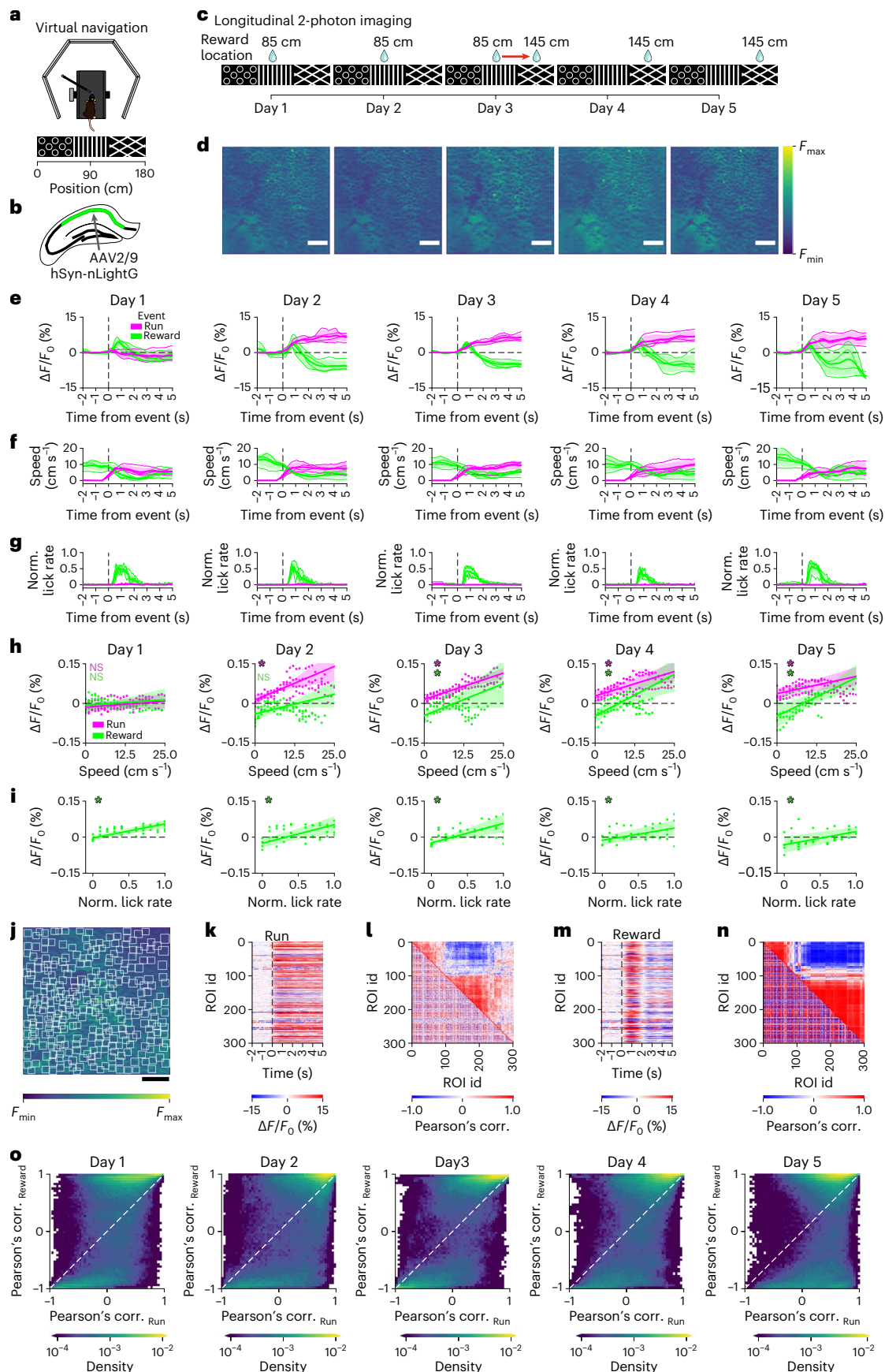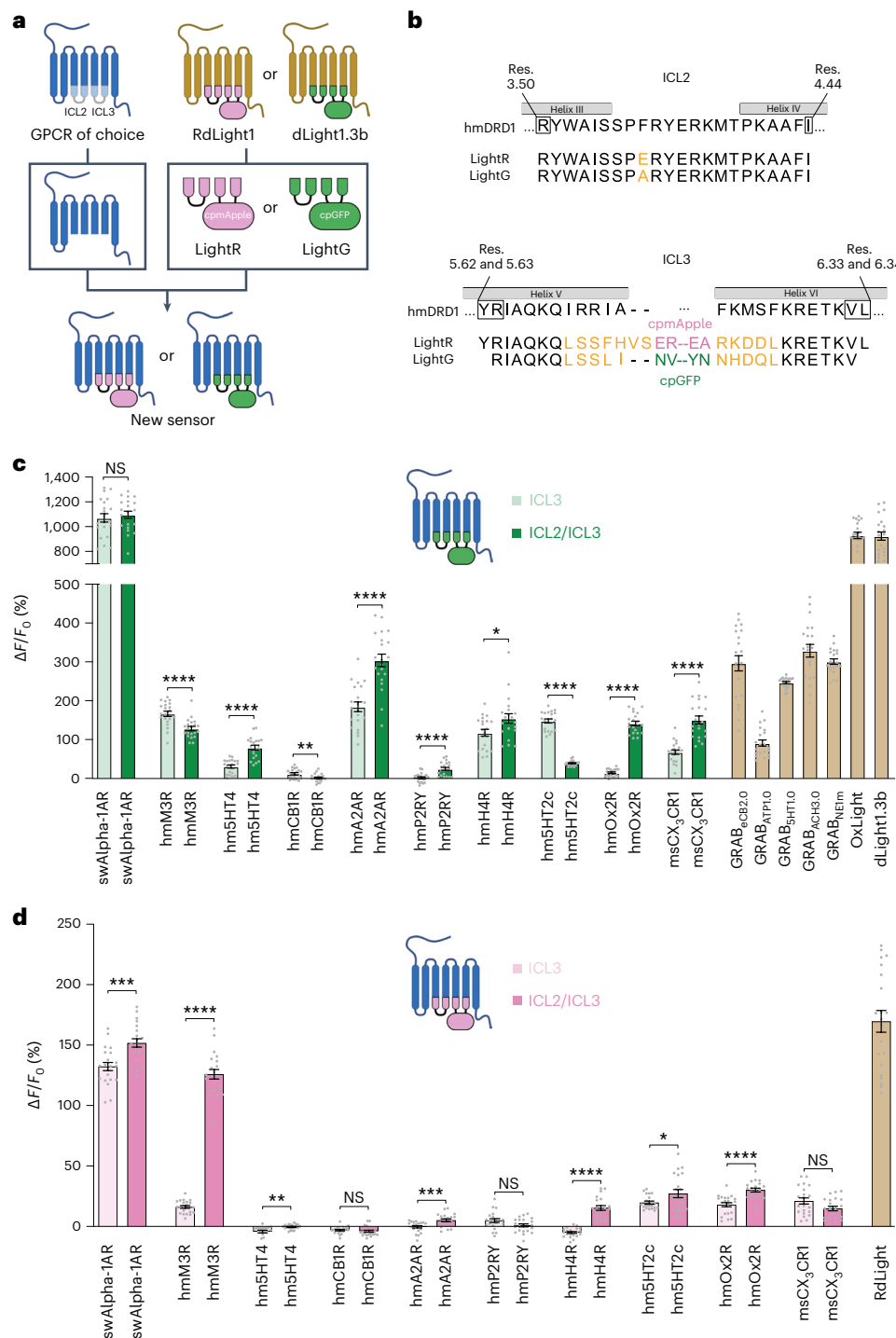
Fig. 5 | Rapid engineering of other multicolor GPCR-indicators. a, Schematic illustration of a strategy for the two-step modular development of multicolor GPCR-based indicators using the LightR and LightG modules. **b**, Aminoacid sequence alignment of the LightG and LightR modules with portions of hmDRD1. Individual residue (Res.) differences between LightR and LightG are highlighted in orange. Helix-forming amino acids of hmDRD1 (according to the AlphaFold[40] structural model of the receptor; Supplementary Fig. 1) are indicated by gray boxes. The initial and terminal residues of the respective LightR and LightG building blocks (black frames) are numbered according to the BW numbering of hmDRD1. **c**, Quantification of the maximal $\Delta F/F_0$ response to bath-applied ligands (all tested at 10 μM concentration) of all generated green indicators. With the exception of msCX3CR1 DG (500 nM) and GRAB$_{ATP1.0}$ (50 μM), for every experiment the ligand was added to a final concentration of 10 μM. The corresponding indicator–ligand pairs used were as follows: swAlpha-1 AR: swAlpha-1 AR, NE; human muscarinic M3 receptor: hmM3R, acetylcholine;

human serotonin 5HT4 receptor: hm5HT4, serotonin; human adenosine 2A receptor: hmA2AR, adenosine; mouse CX3CR1 receptor: msCX3CR1, mouse fractalkine; GRAB$_{eCB2.0}$, 2-arachidonyl glycerol ether; GRAB$_{ATP1.0}$, ATP; GRAB$_{5HT1.0}$, 5HT; GRAB$_{Ach3.0}$, acetylcholine; GRAB$_{NE1m}$, NE; OxLight1, Orexin-A; dLight1.3b, DA. Mean $\Delta F/F_0$ values of single graft (only ICL3 replaced by grafting) and double-graft (ICL3 and ICL2 replaced by grafting) for each receptor were compared using a two-tailed Students t-test with Welch's correction. P values (from left to right): 0.566 (NS); ****7.342 × 10^{-5}; ****6.466 × 10^{-8}; **4.143 × 10^{-3}; ****8.298 × 10^{-7}; ****1.355 × 10^{-5}; *2.072 × 10^{-2}; ****3.629 × 10^{-16}; ****1.748 × 10^{-17}; ****8.324 × 10^{-8}. **d**, Same as in **c** for red indicators. RdLight response was measured with 10 μM DA. P values (from left to right): ***2.625 × 10^{-4}; ****2.910 × 10^{-19}; **3.019 × 10^{-3}; 0.477 (NS); ***9.690 × 10^{-4}; 5.954 × 10^{-2} (NS); ****2.124 × 10^{-10}; *4.593 × 10^{-2}; ****6.331 × 10^{-6}; 6.032 × 10^{-2} (NS). **c,d**, n = 21 cells from three independent experiments for each indicator. Data are shown as mean ± s.e.m.

Finally, we segmented the FOV into anatomically identified regions-of-interest (ROIs) centered on putative cells using a machine learning algorithm[30] (Fig. 4j and Extended Data Fig. 8). We extracted event-triggered averages of nLightG signals for each identified ROI based on the time at which the mouse started to run (Fig. 4k) and based on the time at which the mouse crossed the reward position (Fig. 4m). We computed the Pearson's correlation value between nLightG signals of pairs of ROIs and built cross-correlation matrices (Fig. 4l,n). Across animals, we found that Pearson's correlation values for the same pair of ROIs tended to differ when the mouse started to run ('Pearson's corr.$_{Run}$' in Fig. 4o) with respect to when it crossed the reward position ('Pearson's corr.$_{Reward}$' in Fig. 4o), suggesting that NE signaling in pairs of localized hippocampal regions is correlated differentially across behavioral conditions. Altogether, these results demonstrate that nLightG can be used to image locomotion-induced and reward position-dependent NE dynamics in combination with two-photon microscopy in the hippocampus of awake head-fixed mice.

Rapid engineering of other GPCR-based indicators

To test whether the two-step protein engineering strategy developed herein (Fig. 5a,b) could be applied broadly, we tested it on ten GPCRs in total (Fig. 5c,d). First, the region between BW residues 5.62/5.63 to 6.33/6.34 (ICL3, single graft) was replaced, followed by the additional region between residues 3.50 and 4.44 (ICL2/ICL3, double-graft). Most of the 40 resulting indicators expressed well in HEK293T cells, with only a few exceptions. Eight out of ten GPCRs (80%) produced green indicators with a large response to ligand application (mean $\Delta F/F_0 > 50\%$) (Fig. 5c). On the other hand, two out of ten GPCRs (including Alpha-1 AR and the acetylcholine M3 receptor) produced red indicators with a large response to ligand application in the range (100–250%) of previously in-vivo-validated red fluorescent GPCR-based indicators (Fig. 5d) [3,4].

A comparison of the basal brightness (F_0) revealed that the LightG- and LightR-based indicators often had a higher brightness in the absence of ligand compared with similar, previously developed indicators[7,9,31,32] (Extended Data Fig. 9a–c). We also assessed whether grafting could affect the apparent affinity for the endogenous ligands by determining the half-maximal effective concentration (EC$_{50}$) for a subset of the best performing indicators. We found the EC$_{50}$ of the endogenous agonists was 203 nM for the green acetylcholine indicator (AchLightG, hmM3R single graft), 16 nM for the red acetylcholine indicator (AchLightR, hmM3R double-graft), 1.2 μM for the green adenosine indicator (AdoLightG, hmA2AR double-graft) and 72 nM for the green histamine indicator (HisLightG, hmH4R double-graft) (Extended Data Fig. 10a–d). The affinity of acetylcholine for AchLightR was approximately 100-fold higher than that reported for previously developed indicators based on the same receptor subtype[33]. To check whether this effect stemmed from the additionally grafted ICL2 region, we titrated the double-graft of AchLightG and measured an EC$_{50}$ of 12 nM. This represents a 17-fold increase in affinity of acetylcholine compared with the single graft, with an EC$_{50}$ similar to that of AchLightR (double-graft), demonstrating that replacing the ICL2 with that of a different receptor can sometimes be used to tune the EC$_{50}$ of an indicator. Overall, these data show that our two-step cloning strategy can in some cases, albeit not always, succeed in developing high-quality GPCR-based indicators.

Discussion

In addition to nLightG and nLightR, we developed indicators for several other neuromodulators. A recent study reported the use of a similar grafting approach for the generation of green GPCR-based indicators[34]. A direct comparison between these two approaches could be performed in the future to establish whether one is more successful than the other.

Our results show that nLightG and nLightR have improved selectivity for NE over DA compared with GRAB$_{NE1m}$. Nevertheless, both indicators showed detectable responses to perfusion of a high (50 μM) DA concentration in brain slices. This suggests that, when planning the use of any of these sensors in areas of the brain with dense dopaminergic innervation (that is the basal ganglia)[35,36], careful experimental design should be put in place to disambiguate the two catecholamines.

A potential limitation of fiber photometry recordings, which has recently gained attention, is the possible occurrence of artefacts caused by animal motion or hemodynamics[25,37,38]. These artefacts typically affect fluorescence signals excited at 405 nm or 470 nm uniformly[38]. To address this issue, our photometry recordings were conducted at both wavelengths, with 405 nm serving as a control channel. A comparison between 470 nm and 405 nm traces revealed that only the 470 nm channel exhibited optogenetically evoked nLightG responses, while these were absent in the 405 nm channel. Therefore, the signals detected in fiber photometry experiments were specific to nLightG responses and were not influenced by hemodynamics or motion artefacts. In two-photon functional imaging experiments, we did not test a loss-of-function approach (for example, a ligand-insensitive version of nLightG). However, structural similarity analysis and temporal shuffling of nLightG traces provided convincing evidence that the observed nLightG signals were not a result of motion-related artifacts.

Our demonstration of in vivo NE detection using nLightG opens several opportunities for future research. First, owing to its pharmacology, nLightG could be used to investigate the effects of clinically used Alpha-2 AR agonists and antagonists on behaviorally evoked NE release in vivo, while GRAB$_{NE1m}$ fails to do so. Second, owing to its fast kinetics, nLightG could be used to precisely investigate the effects of different conditions on NE dynamics, for example, the use of clinically relevant drugs such as antidepressants and psychostimulants or genetic manipulations, both during natural animal behavior or optogenetic stimulation. Finally, given its compatibility with two-photon imaging, nLightG could be used to chart spatial and temporal aspects of NE signaling in previously unexplored cortical and subcortical areas. Thus the next-generation of NE indicators introduced here greatly advances the neurotechnological toolbox that is necessary to investigate the physiological functions of the NE system with high spatiotemporal resolution.

Online content

Any methods, additional references, Nature Portfolio reporting summaries, source data, extended data, supplementary information, acknowledgements, peer review information; details of author contributions and competing interests; and statements of data and code availability are available at https://doi.org/10.1038/s41592-023-01959-z.

References

1. Labouesse, M. A. & Patriarchi, T. A. A versatile GPCR toolkit to track in vivo neuromodulation: not a one-size-fits-all sensor. *Neuropsychopharmacology* **46**, 2043–2047 (2021).
2. Wu, Z., Lin, D. & Li, Y. Pushing the frontiers: tools for monitoring neurotransmitters and neuromodulators. *Nat. Rev. Neurosci.* **23**, 257–274 (2022).
3. Patriarchi, T. et al. An expanded palette of dopamine sensors for multiplex imaging in vivo. *Nat. Methods* **17**, 1147–1155 (2020).
4. Sun, F. et al. Next-generation GRAB sensors for monitoring dopaminergic activity in vivo. *Nat. Methods* **17**, 1156–1166 (2020).
5. Sara, S. J. The locus coeruleus and noradrenergic modulation of cognition. *Nat. Rev. Neurosci.* **10**, 211–223 (2009).
6. Aston-Jones, G. & Cohen, J. D. An integrative theory of locus coeruleus-norepinephrine function: adaptive gain and optimal performance. *Annu. Rev. Neurosci.* **28**, 403–450 (2005).
7. Feng, J. et al. A genetically encoded fluorescent sensor for rapid and specific in vivo detection of norepinephrine. *Neuron* **102**, 745–761.e8 (2019).

8. Patriarchi, T. et al. Ultrafast neuronal imaging of dopamine dynamics with designed genetically encoded sensors. *Science* **360**, eaat4422 (2018).

9. Duffet, L. et al. A genetically encoded sensor for in vivo imaging of orexin neuropeptides. *Nat. Methods* **19**, 231–241 (2022).

10. Hauser, A. S. et al. GPCR activation mechanisms across classes and macro/microscales. *Nat. Struct. Mol. Biol.* **28**, 879–888 (2021).

11. Cvicek, V., Goddard, W. A. & Abrol, R. Structure-based sequence alignment of the transmembrane domains of all human GPCRs: phylogenetic, structural and functional implications. *PLoS Comput. Biol.* **12**, e1004805 (2016).

12. Ballesteros, J. A. & Weinstein, H. in *Methods in Neurosciences* Vol. 25 (ed. Sealfon, S. C.) 366–428 (Academic Press, 1995).

13. Kubitschke, M. et al. Next generation genetically encoded fluorescent sensors for serotonin. *Nat. Commun.* **13**, 7525 (2022).

14. Chen, T.-W. et al. Ultrasensitive fluorescent proteins for imaging neuronal activity. *Nature* **499**, 295–300 (2013).

15. Wu, D., Katz, A., Lee, C. H. & Simon, M. I. Activation of phospholipase C by alpha 1-adrenergic receptors is mediated by the alpha subunits of Gq family. *J. Biol. Chem.* **267**, 25798–25802 (1992).

16. Nehmé, R. et al. Mini-G proteins: novel tools for studying GPCRs in their active conformation. *PLoS ONE* **12**, e0175642 (2017).

17. Dixon, A. S. et al. NanoLuc complementation reporter optimized for accurate measurement of protein interactions in cells. *ACS Chem. Biol.* **11**, 400–408 (2016).

18. Morris, D. P., Price, R. R., Smith, M. P., Lei, B. & Schwinn, D. A. Cellular trafficking of human α1a-adrenergic receptors is continuous and primarily agonist-independent. *Mol. Pharmacol.* **66**, 843–854 (2004).

19. Chalothorn, D. et al. Differences in the cellular localization and agonist-mediated internalization properties of the α1-adrenoceptor subtypes. *Mol. Pharmacol.* **61**, 1008–1016 (2002).

20. Stanasila, L., Abuin, L., Dey, J. & Cotecchia, S. Different internalization properties of the α1a- and α1b-adrenergic receptor subtypes: the potential role of receptor interaction with β-arrestins and AP50. *Mol. Pharmacol.* **74**, 562–573 (2008).

21. Nörenberg, W., Schöffel, E., Szabo, B. & Starke, K. Subtype determination of soma-dendritic alpha2-autoreceptors in slices of rat locus coeruleus. Naunyn Schmiedebergs. *Arch. Pharm.* **356**, 159–165 (1997).

22. Starke, K., Göthert, M. & Kilbinger, H. Modulation of neurotransmitter release by presynaptic autoreceptors. *Physiol. Rev.* **69**, 864–989 (1989).

23. Simson, P. E. & Weiss, J. M. Alpha-2 receptor blockade increases responsiveness of locus coeruleus neurons to excitatory stimulation. *J. Neurosci.* **7**, 1732–1740 (1987).

24. Park, J., Kile, B. M. & Mark Wightman, R. In vivo voltammetric monitoring of norepinephrine release in the rat ventral bed nucleus of the stria terminalis and anteroventral thalamic nucleus. *Eur. J. Neurosci.* **30**, 2121–2133 (2009).

25. Formozov, A., Dieter, A. & Wiegert, J. S. A flexible and versatile system for multi-color fiber photometry and optogenetic manipulation. *Cell Rep. Methods* **3**, 100418 (2023).

26. Chandler, D. J. et al. Redefining noradrenergic neuromodulation of behavior: impacts of a modular locus coeruleus architecture. *J. Neurosci.* **39**, 8239–8249 (2019).

27. Jones, B. E., Halaris, A. E., McIlhany, M. & Moore, R. Y. Ascending projections of the locus coeruleus in the rat. I. Axonal transport in central noradrenaline neurons. *Brain Res.* **127**, 1–21 (1977).

28. Kaufman, A. M., Geiller, T. & Losonczy, A. A role for the locus coeruleus in hippocampal CA1 place cell reorganization during spatial reward learning. *Neuron* **105**, 1018–1026.e4 (2020).

29. Gray, S. R., Ye, L., Ye, J. Y. & Paukert, M. Noradrenergic terminal short-term potentiation enables modality-selective integration of sensory input and vigilance state. *Sci. Adv.* **7**, eabk1378 (2021).

30. Sità, L. et al. A deep-learning approach for online cell identification and trace extraction in functional two-photon calcium imaging. *Nat. Commun.* **13**, 1529 (2022).

31. Dong, A. et al. A fluorescent sensor for spatiotemporally resolved imaging of endocannabinoid dynamics in vivo. *Nat. Biotechnol.* **40**, 787–798 (2022).

32. Wu, Z. et al. A sensitive GRAB sensor for detecting extracellular ATP in vitro and in vivo. *Neuron* **110**, 770–782.e5 (2022).

33. Jing, M. et al. An optimized acetylcholine sensor for monitoring in vivo cholinergic activity. *Nat. Methods* **17**, 1139–1146 (2020).

34. Ino, D., Tanaka, Y., Hibino, H. & Nishiyama, M. A fluorescent sensor for real-time measurement of extracellular oxytocin dynamics in the brain. *Nat. Methods* **19**, 1286–1294 (2022).

35. Rice, M. E., Patel, J. C. & Cragg, S. J. Dopamine release in the basal ganglia. *Neuroscience* **198**, 112–137 (2011).

36. Liu, C., Goel, P. & Kaeser, P. S. Spatial and temporal scales of dopamine transmission. *Nat. Rev. Neurosci.* **22**, 345–358 (2021).

37. Marshall, J. D. et al. Cell-type-specific optical recording of membrane voltage dynamics in freely moving mice. *Cell* **167**, 1650–1662.e15 (2016).

38. Zhang, W.-T. et al. Spectral fiber photometry derives hemoglobin concentration changes for accurate measurement of fluorescent sensor activity. *Cell Rep. Methods* **2**, 100243 (2022).

39. Mirdita, M. et al. ColabFold: making protein folding accessible to all. *Nat. Methods* **19**, 679–682 (2022).

40. Jumper, J. et al. Highly accurate protein structure prediction with AlphaFold. *Nature* **596**, 583–589 (2021).

Methods

Molecular cloning

DNA sequences encoding individual GPCRs and GRAB indicators were either obtained from Addgene (GRAB$_{ACh3.0}$, catalog no. 121922; GRAB$_{5HT1.0}$, catalog no. 140552; GRAB$_{ATP1.0}$, catalog no. 167577; GRAB$_{eCB2.0}$, catalog no. 164604) or directly ordered as gene fragments (Twist Bioscience, ThermoFisher Scientific) and cloned into a mammalian expression vector downstream of a CMV-promoter (Addgene plasmid catalog no. 60360) by restriction enzyme cloning using *Not*I and *Hin*dIII sites. Cloning of DNA sequences from dLight1.3b or RdLight1 (University of Zurich Viral Vector Facility (UZH-VVF)) onto individual GPCRs for the generation of single graft and double-graft constructs was performed by Gibson Assembly using the NEBuilder HiFi DNA Assembly Master Mix (New England Biolabs). A list of primers used can be found in Supplementary Data 1. Site-directed mutagenesis was performed by PCR using custom-designed primers (ThermoFisher Scientific) and PfuUltra II Hotstart PCR Master Mix (Agilent). To generate C-terminal fusions of SmBit onto DRD1, swAlpha-1 AR, nLightG and nLightR, the SmBit sequence was PCR-amplified from the pCMV-Beta2AR-SmBit plasmid and cloned in place using Gibson assembly. All sequences were verified using Sanger sequencing (Microsynth). The DNA sequences encoding nLightG and nLightR were cloned into a viral vector under the control of a human Synapsin-1 promoter (UZH-VVF) by restriction enzyme cloning using *Bam*HI and *Hin*dIII sites.

Cell culture, confocal imaging and quantification

HEK293T cells (ATCC catalog no. CRL-3216) were cultured as previously described[9]. The cell line was authenticated by the commercial provider. Cells were transfected at 40–50% confluency in glass-bottomed dishes or six-well plates using PolyFect Transfection Reagent (Qiagen) according to manufacturer instructions, and used for follow-up experiments 24–48 h after transfection. Primary cortical neurons were prepared using the following procedure: the cerebral cortex of rat embryos at 18 days of gestation was meticulously dissected and rinsed with 5 ml of sterile-filtered PBGA buffer, which consisted of PBS with 10 mM glucose, 1 mg ml^{-1} bovine serum albumin and a 1:100 dilution of antibiotic-antimycotic solution (10,000 units ml^{-1} penicillin; 10,000 µg ml^{-1} streptomycin; 25 µg ml^{-1} amphotericin B) from ThermoFisher Scientific. The cortices were then cut into small fragments and incubated in 5 ml of sterile-filtered papain solution at 37 °C for 15 min. Afterward, the tissues were washed with complete DMEM medium containing 10% fetal calf serum, penicillin/streptomycin (1:100), and further dissociated by trituration. The resulting cell suspension was filtered through a 40-µm cell strainer. The neurons were plated at a density of 40,000–50,000 cells per well on poly-L-lysine-coated dishes (50 µg ml^{-1} in PBS, ThermoFisher Scientific) and cultured in NU-medium, which consisted of Minimum Essential Medium (MEM) supplemented with 15% NU serum, 2% B27 supplement, 15 mM HEPES, 0.45% glucose, 1 mM sodium pyruvate and 2 mM GlutaMAX. After 4–6 days, the cultures were transduced with adeno-associated viruses (AAVs) at a final titer of 1 × 10^9 GC ml^{-1} and maintained for 12–16 days in vitro. All cells were imaged at room temperature in glass bottom dishes using Hank's Balanced Salt Solution (HBSS) containing CaCl$_2$ and MgCl$_2$ from ThermoFisher Scientific. For live-cell labeling, cells were incubated with Alexa-647-anti-FLAG antibody (1:1,000) for 10 min at room temperature and washed twice with PBS. Imaging was performed using Zen Blue software on an inverted Zeiss LSM 800 confocal microscope equipped with 488 nm laser (for green indicators) or a 561 nm laser (for red indicators), using either a ×20 air-based or a ×40 oil-based objective. During timelapse imaging, ligands were applied manually using a pipette to reach the specified final concentrations. For quantification of the fluorescence response $\Delta F/F_0$, ROIs that enclose isolated cell membranes were selected manually using the threshold function of Fiji (ImageJ). The fluorescence response of an indicator ($\Delta F/F_0$) was calculated as follows: $(F_t - F_0)/F_0$

with F_t being the ROI mean gray value at each time point t, and F_0 being the mean gray value of the ten timepoints immediately before ligand addition.

Plate reader-based assays

For measuring dose-responses to titrations of ligands on the indicators, HEK293T cells were transfected in a T75 flask using polyethyleneimine hydrochloride (PEI, Sigma-Adlrich). For each flask 432 µl of PBS (ThermoFisher Scientific) supplemented with 150 mM of NaCl was mixed with 48 µl of PEI solution (1 mg ml^{-1}, pH 7.0 in ddH$_2$O) and 9 µg of plasmid DNA was added before vortexing. The transfection mixture was incubated at RT for 45 min and added to the cells in a dropwise manner. The medium was replaced 24 h after transfection and the cells were used for titrations 48 h after transfection. The cells were detached using Versene (ThermoFisher Scientific), centrifuged (RT; 150g; 3 min), washed and resuspended in HBSS to a density of 6.66 × 10^6 cells ml^{-1}. The wells of a black, flat-bottom, 96-well plate (Greiner Bio-One) were filled with 150 µl of cell suspension and to each well 150 µl of a twofold concentrated dilution series of ligand in HBSS was added. The fluorescence signal was detected at room temperature using a Tecan M200 Pro plate reader with an excitation wavelength of 480 nm or 560 nm (bandwidth of 9 nM) and an emission wavelength of 560 nm or 600 nM (bandwidth of 35 nM) for the green and the red indicators, respectively. For each titration series, three biological replicates were measured and the normalized means were fitted with a four-parameter dose-response curve to determine the EC$_{50}$.

For measuring the one-photon excitation and emission spectra of the indicators, HEK293T cells were transfected using PolyFect® Transfection Reagent (Qiagen) according to manufacturer's instructions and used for spectral measurements 48 h after transfection. The cells were plated in two wells of a black, flat-bottom, 96-well plate as described above. To account for the autofluorescence of the cells, a nontransfected control was measured at the exact same conditions. One-photon fluorescence excitation (λ_{em} = 560 nm or 620 nm for green and red indicators, respectively) and emission (λ_{exc} = 470 nm or 550 nm for green and red indicators, respectively) spectra were determined on a Tecan M200 Pro plate reader at room temperature.

To measure the recruitment of G-proteins and β-arrestin-2 we used a NanoBiT complementation-based assay[17]. For this we used the wild-type swAlpha-1 AR, an hmDRD1 receptor or the NE indicators carrying a C-terminally fused SmBiT fragment in combination with either mini-G-protein probes (mini-Gs, mini-Gi and mini-Gq[41]) or β-arrestin-2 (ref. [42]) N-terminally fused to LgBiT, as specified. HEK293T cells were seeded in six-well-plates (Techno Plastic Products) at a density of 250,000 cells pre well and cotransfected using PolyFect with the above-mentioned constructs at a 1:1 DNA ratio. Cells were detached using Versene 24 h after transfection, centrifuged (RT, 150g, 3 min), washed and resuspended (0.5 × 10^6 cells ml^{-1}) in Fluorobrite–DMEM (ThermoFisher Scientific) complemented with 30 mM of HEPES (ThermoFisher Scientific). For each interaction pair, 200 µl of the cell suspension were gently mixed with 50 µl of a 20-fold dilution of Nano-Glo reagent in LCS buffer (Promega) and distributed equally into two wells of a white flat-bottom 96-well plate OptiPlate (PerkinElmer) before incubation at 37 °C for 45 min. The luminescence signal was measured at 37 °C using a Tecan Spark plate reader before and after the manual addition of 25 µl ligand solution (10 µM final concentration) in Fluorobrite–DMEM in one well or 25 µl of pure Fluorobrite–DMEM in the other well.

Patch-clamp fluorometry

To analyze the response kinetics of nLightG and GRAB$_{NE1m}$ we used patch-clamp fluorometry similar to our previously described procedure[13]. Outside-out membrane patches derived from HEK cells expressing nLightG or GRAB$_{NE1m}$ were positioned in front of a double-barreled perfusion pipette, which was moved swiftly using a piezo actuator[43].

Fluorescence was captured using an EMCCD (electron multiplying charge coupled device) camera. HEK293T cells were cultured on poly-D-lysine/laminin-coated glass coverslips in DMEM with 7% FBS at 37 °C and 5% CO_2 to minimize background fluorescence. Transfections were performed after 24 h using polyethylenimine 25,000 (Sigma) with approximately 0.3 µg DNA per milliliter medium. After 72 h of expression, coverslips containing the adherent cells were immersed in an external solution (138 mM NaCl, 1.5 mM KCl, 1.2 mM $MgCl_2$, 2.5 mM $CaCl_2$, 10 mM HEPES, pH 7.3), and membrane patches were generated by pulling borosilicate glass patch pipettes (G150TF-4, Warner Instruments; resistance: 4–6 MΩ) filled with internal solution (135 mM K-gluconate, 10 mM NaCl, 2 mM $MgCl_2$, 1 mM EGTA, 10 mM HEPES, pH 7.3). Cell-attached and whole-cell configurations were established using a Patchstar micro-manipulator (Scientifica) and Axopatch 200B patch-clamp amplifier (Molecular Devices) to excise outside-out patches. The experiments were conducted at room temperature. Voltage pulses for ligand application and camera triggering were generated using pClamp 10.7 and the Digidata 1550 A/D converter (both Molecular Devices). Epifluorescence imaging of the excised patches was performed on an inverse DMi8 microscope (Leica) with a ×20 objective (HC PL FLUOTAR L ×20/0.40 CORR PH1). Green fluorescence was excited using a 470 nm LED (Thorlabs) and a 470/40 nm excitation filter in combination with a 495 nm dichroic mirror and a 525/50 nm emission filter (all Chroma). The light intensity in the focal plane was approximately 2–10 mW mm^{-2}. Images were captured using an Evolve 512 delta EMCCD camera (Photometrics) with the assistance of MicroManager2.0 (ref. 44). The acquisition of individual frames (camera clearing mode: presequence; acquisition mode: strobed) was triggered by transistor-transistor logic pulses provided by pClamp. Imaging was conducted at a frame rate of 100 fps (cropping to 256 × 256 pixels, 2 × 2 binning, 9 ms exposure, EM gain 200) or 200 fps (cropping to 256 × 256 pixels, 2 × 2 binning, 4.5 ms exposure, EM gain 500). Rapid ligand application and removal were achieved by placing the outside-out patches in front of a piezo-driven double-barreled Θ-glass pipette[43]. The perfusion pipette was created from borosilicate glass (outer diameter: 2.0 mm, inner diameter: 1.40 mm, septum: 0.2 mm, Warner Instruments), broken to yield a tip with a diameter of approximately 250 µm, and connected to a piezo actuator (P842.20, Physik Instrumente). Lateral displacements were triggered by short voltage steps (3 V ramp in 0.7), amplified using a power supply (E505.10, Physik Instrumente) and filtered at 1 kHz. Solutions were delivered using a syringe pump (0.3 ml min^{-1} per channel) with parallel bath perfusion at approximately 3–5 ml min^{-1}. NE (5 µM, Sigma catalog no. 74480) in external solution (1.2-fold concentrated to obtain exchange currents) was applied in 1 s or 2 s pulses. Fiji[45] (ImageJ) was used to calculate $\Delta F/F_0$ maps based on mean intensity projections of 100 frames before and 100 frames during NE application (Fig. 2g). These maps were used to define the responsive patch region and placing of a rectangular ROI. The fluorescence intensity of this region was exported and normalized to the initial background fluorescence obtained from an adjacent region. Figure 2i shows six subsequent applications interrupted by 0.2 s breaks in the imaging/illumination sequence (white spaces). In this case, a baseline correction was performed (dashed line) to account for minor signal loss in the patch region ($0.72 e^{-t} 40 s^{-1}$). However, consecutive applications showed full reversibility of the signal changes (Supplementary Video 1). To obtain estimates of the response times, data from four to six consecutive applications were averaged from each patch and single-exponential fits were used to determine τ_{on} and τ_{off} time constants by least-square fitting with ProFit v.7.0 (Quantumsoft).

In vitro two-photon brightness measurements

Two-photon spectral characterizations of the nLightG indicator were performed on HEK293T cells before and after addition of NE (100 µM). Cells were transfected using Lipofectamine 3000 and imaged 24 h posttransfection. Before the spectral measurements the medium was switched to PBS to avoid DMEM autofluorescence. Two-photon spectra were acquired as described previously[9].

Viral production

AAVs encoding the indicators developed in this study were produced by the UZH-VVF. All other viruses were obtained either from the UZH-VVF or Addgene. The titers of the viruses used in this study were: rAAV2/9.hSynapsin1.nLightR, 1.4×10^{13} GC ml^{-1}; rAAV2/9.hSynapsin1.nLightG, 2.3×10^{13} GC ml^{-1}; rAAV2/9.hSynapsin1.GRAB$_{NE1m}$, 5.5×10^{12} GC ml^{-1}; rAAV2/5-hEF1α.DIO.ChrimsonR-tdTomato, 4.7×10^{12} GC ml^{-1}; rAAV2/9.EF1α.DIO.ChrimsonR-mRuby2, 4.5×10^{12} GC ml^{-1}.

Animals

Animal procedures were performed in accordance to the guidelines of the European Community Council Directive or the Animal Welfare Ordinance (TSchV 455.1) of the Swiss Federal Food Safety and Veterinary Office and were approved by the Zürich Cantonal Veterinary Office, the Hamburg state authority for animal welfare and the animal welfare officer of the University Medical Center Hamburg-Eppendorf, National Council on Animal Care of the Italian Ministry of Health. Rat embryos (E17) obtained from timed-pregnant Wistar rats (Envigo) were used for preparing primary cortical neuronal cultures. Wild-type C57BL/6 mice, heterozygous B6.Cg-Dbhtm3.2(cre)Pjen/J (DBH-Cre) mice[46] and heterozygous C57BL/6-Tg(Dbh-iCre)1Gsc (DBH-iCre) mice[47] of both sexes were used in this study. Mice were kept with ad libitum access to chow and water on a 12-h reversed light–dark cycle. Optogenetic and behavior experiments were performed during the dark phase. Two-photon imaging experiments were performed on animals older than 10 weeks that were housed at room temperature and in humidity-controlled rooms in groups of up to five littermates per cage with ad libitum access to food and water in a 12-h light–dark cycle.

Animal surgeries and viral injections

Surgeries were conducted on adult anesthetized mice (males and females, age >6 weeks). For slice imaging experiments, AAVs encoding nLightG, nLightR or GRAB$_{NE1m}$[7] under the control of the human synapsin-1 promoter were unilaterally injected at a titer of ~5.5×10^{12} GC ml^{-1} into the LH (−1.4 mm anteroposterior (AP), +1.1 mm mediolateral (ML), −5.2 mm dorsoventral (DV); volume, 600 nl). For single-site in vivo photometry experiments, the following AAVs were unilaterally injected at a similar titer into either of the following regions: LH (−1.4 mm AP, +1.1 mm ML, −5.2 mm DV; volume, 250 nl), vHPC (−3.2 mm AP, −3.3 mm ML, −3.8 mm DV; volume, 250 nl) and commercial fiber optic cannulas were then implanted 0.1–0.2 mm above the injection sites (for LH, 400 µm core diameter, numerical aperture (NA) = 0.57, Doric lenses; for vHPC, 200 µm core diameter, NA = 0.37, Neurophotometrics). Mice used for optogenetic stimulation experiments also received an unilateral injection (1,000 nl) in LC of undiluted rAAV2/5-hEF1α.DIO.ChrimsonR-tdTomato and were implanted an additional fiber optic cannula above the injection site. For dual-site in vivo photometry experiments, to bilaterally access the LC and dHPC, small craniotomies (~500 µm diameter) were drilled −5.4 mm posterior and ±1.1 mm lateral to Bregma (to access LC) as well as −2 mm posterior and ±1.5 mm lateral to Bregma (to access dHPC). Then, 300 nl of viral suspension consisting of a mixture of rAAV2/9.hSynapsin1.nLightG (~1.2×10^{13} GC ml^{-1}) and rAAV2/9.EF1α.DIO.ChrimsonR-mRuby2 (~4.5×10^{12} GC ml^{-1}) were injected into each LC at a depth of −3.6 mm. Subsequently, 500 nl of rAAV2/9.hSynapsin1.nLightG (~1.2×10^{13} GC ml^{-1}) was injected into each dHPC at a depth of −1.6 mm. After each injection, the pipette was left in place for ~2 min, before being slowly withdrawn. After pipette withdrawal, fiber optic cannulas (400 µm core diameter, NA = 0.5, RWD) were slowly inserted at the injection coordinates to a depth of −3.5/−1.2 mm.

For two-photon imaging, neuronal-specific expression of nLightG was obtained by injecting rAAV2/9.hSynapsin1.nLightG into the

hippocampal CA1 region (−1.75 mm AP, +1.35 mm ML, −1.40 mm DV) through a craniotomy opened in the right hemisphere. AAV solution (800 nl) was injected using an injection apparatus (UltraMicroPump, World Precision Instruments). Following viral injection, a chronic hippocampal window was implanted following described procedures[48–50]. In brief, a 3 mm trephine-drill was used to open a craniotomy centered at coordinates 2.00 mm posterior and 1.80 mm lateral to bregma. Optical access to the hippocampus was obtained removing the overlying cortical tissue by careful aspiration. Throughout the aspiration procedure, the brain tissue was continuously flushed with HEPES-buffered artificial cerebrospinal fluid. To enable optical access, an optical window was affixed to the craniotomy above the external capsule, and a thin layer of silicone elastomer (Kwik-Sil, World Precision Instruments) was positioned between the brain tissue and the surface of the optical window. Using epoxy glue, a customized titanium headplate was securely attached to the skull, and dental cement (Super-Bond, Sun Medical) was employed to further stabilize the implant components. Finally, the scalp incision was sutured to ensure proper adherence to the implant. At the conclusion of the surgery, animals were administered an intraperitoneal bolus of antibiotics (BAYTRIL, Bayer). Optical windows were constructed following previously described methods[48], involving the use of a thin-walled stainless-steel cannula segment (outer diameter: 3 mm; inner diameter: 2.77 mm; height: 1.50–1.60 mm) and a round coverslip with a diameter of 3.00 mm. The coverslip was securely fastened to the lower end of the cannula using ultraviolet-curable optical epoxy (Norland optical adhesive 63, Norland). All virus injections were conducted at a rate of approximately 100 nl min^{-1}.

Acute brain slice preparation, imaging and quantification

For acute brain slice preparation, at least 4 weeks after bilateral viral injections, mice were deeply anesthetized with an intraperitoneal injection of pentobarbital (200 mg kg^{-1}, 10 ml kg^{-1}) and perfused intracardially with ice-cold artificial cerebrospinal fluid (aCSF) bubbled with 95/5% O$_2$/CO$_2$ containing 120 mM NaCl, 2.5 mM KCl, 1.25 mM NaH$_2$PO$_4$, 26 mM NaHCO$_3$, 5 mM HEPES, 1 mM MgCl$_2$, 14.6 mM D-glucose and 2.5 mM CaCl$_2$ (Osmolarity: 305–310 mOsm kg^{-1}). After perfusion, mice were decapitated and the brain was quickly extracted while submerged in the ice-cold aCSF. Coronal slices (250–300 μm thick) containing the LHA were obtained using a vibratome (HM 650V, ThermoFisher Scientific). The slices were incubated at 34 °C for 20 min in continuously oxygenated aCSF. Following incubation, brain slices were transferred at room temperature and kept until recording. Recordings were conducted in a slice chamber kept at 31 °C perfused with aCSF. For electrical stimulation at 20 Hz, a bipolar electrode (Parallel Bipolar, 30211, FHC) was positioned near the LHA. Electrical stimuli were synchronized by using Pulse Pal (Open Ephys). To visualize green or red NE indicators, slices were illuminated with either a blue (469 nm) or green (555 nm) LED (Colibri 7, Zeiss), respectively, on an upright Axio Examiner A1 microscope (Zeiss) using an N-Achroplan ×10/0.3 M27 objective (Zeiss). Images were collected at a sample rate of 5 Hz for nLightG and GRAB$_{NE1m}$ of 2 Hz for nLightR (Live Acquisition, ThermoFisher Scientific). The stimulation voltage was set at 2.5 V and the duration of each stimulation was 10 ms. The train duration of each session determined the number of pulses delivered to each slice. For pharmacological experiments, drugs were applied via a perfusion system at a flow rate at 2.5 ml min^{-1} and images were recorded at a 0.5 Hz sample rate for nLightG and GRAB$_{NE1m}$ and at 0.2 Hz for nLightR.

The analysis of slice imaging data was performed using a custom-written MATLAB v.R2019b script. ROIs of equal size were selected for each slice using Fiji (ImageJ). For both electrical stimulation and ligand-perfusion experiments, the change in fluorescence $\Delta F/F_0$ (%), defined as $(F − F_0)/F_0 \times 100$ was calculated. F_0 was defined using a 1 s baseline for both the nLightG and GRAB$_{NE1m}$ and a 2.5 s baseline for nLightR. Depending on the rate and pattern of photobleaching, signals were fitted with either the MATLAB polyfit polynomial function

of fourth degree or with the exp1 single-term exponential function and detrended using the detrend function. $\Delta F/F_0$ (%) signals for each indicator acquired from electrical stimulation experiments were averaged and smoothed with a three-point moving mean filter. Peaks responses were calculated as maximum $\Delta F/F_0$ (%) response to each stimulation. For all the ligand-perfusion experiments 2-min bins were defined for each drug/condition (DA, NE, NE+Trz perfusions and NE washout) for mean $\Delta F/F_0$ (%) calculations. Representative traces were smoothed with a three-point (for selectivity experiments) or a five-point (for NE washout experiments) moving mean filter.

Fiber photometry

Recordings in lateral hypothalamus during tail-lifting. Fiber photometry recordings in the LH were performed using an iFMC6_IE(400-410)_E1(460-490)_F1(500–540)_E2(555-570)_F2(580–680)_S photometry system (Doric Lenses) controlled by the Doric Neuroscience Studio v.6.1.2.0 software. A low-autofluorescence patch cord (400 μm, 0.57 NA, Doric Lenses) was attached to the ferrule on mouse's head and used to excite nLightG and GRAB$_{NE1m}$ (465 nm) or nLightR (560 nm) and collect the fluorescence emission, while 405 nm was used as a control fluorescence signal for all the indicators. Signals were modulated sinusoidally at 208 Hz and 572 Hz (405 nm and 465 nm, respectively) and at 333 Hz (560 nm) via lock-in amplification, then demodulated online and low-passed filtered at 12 Hz. Mice were habituated to handling, injections and tethering before all fiber photometry experiments. Experiments started 4 weeks after surgery to allow proper expression of the indicators. A baseline period of the fluorescent signal was recorded before drug administration and for 5 min after the injection of saline (0.9% NaCl, 10 μl g^{-1} bodyweight) or drug solution. Yoh (Y3125-1G; Sigma Aldrich) was diluted in saline to 4 μg g^{-1} bodyweight for i.p. injection (10 μl g^{-1}). Trz (T6154-1G; Sigma Aldrich) was diluted in saline to 10 μg g^{-1} bodyweight for i.p. injection (10 μl g^{-1}). After i.p. injection, signals were recorded for an additional 5 min before the tail-lifting task was performed. Each mouse was lifted by the tail five times of 1-min duration each, while indicator fluorescence was recorded. Between each tail lift mice had 2-min intervals in the experimental cage.

Recordings in vHPC during optogenetic stimulation. The fluorescence signal emitted by NE indicators nLightG and GRAB$_{NE1m}$, exhibiting a green fluorescence, was captured using a commercially available photometry system (Neurophotometrics, Model FP3002). The system was controlled through the utilization of Bonsai, an open-source software (v.2.6.2). For delivering interleaved excitation light, two LEDs were employed: a 470 nm LED for recording NE-dependent fluorescent signals (F470), and a 415 nm LED for control fluorescent signals (F415). Both LEDs were set to a sampling rate of 120 Hz, enabling each channel to operate at 60 Hz. The power of excitation at the fiber tip was adjusted to 25–35 μW. Throughout the recording session, mice were anesthetized using 4% isoflurane during induction and 1.5–2% during maintenance. The fiber, which was implanted in the mouse brain, was connected to a prebleached recording patch cord (200 μm, 0.39 NA) provided by Doric Lenses. For Yoh injection (10 μl g^{-1}, 4 mg kg^{-1}), a catheter was placed i.p. During the photometry recording session, an LC stimulation sequence was performed pre- and 15 min post-Yoh injection. Each sequence consisted of three LC optical stimulations for 10 s each (5 Hz, 10 ms pulse width, 635 nm CNI laser at 10 mW output power) with 2 min interstimulation intervals.

Simultaneous dual-site recordings in LC and dHPC during optogenetic stimulation. At 3–4 weeks after surgery, animals were habituated to the experimenter by daily handling for a couple of days, before being habituated to the setup and to head-fixation on a linear treadmill (200–100 500 2100 and 700–100 100 0010; Luigs & Neumann). Fiber photometry recordings were realized using the PyPhotometry[51] system: the PyPhotometry-board controlled a multicolor light source

(pE-4000; CoolLED) connected to the 400–480 nm port of a dichroic cube (FMC5_E1(400–480)_F1(500–540)_E2(555-570)_F2(580–680)_S; Doric Lenses). Excitation light was bandpass filtered at 405/10 nm (catalog no. 65-133, Edmund optics) and 470/10 nm (catalog no. 7394, Alluxa) and delivered in a temporally interleaved manner[51]. Excitation power was adjusted such that the emission intensities of nLightG were similar when excited at 405 and 470 nm, respectively. Emission light was measured at the 500–540 nm port using a photodetector (DFD_FOA_FC; Doric Lenses), and digitized by the PyPhotometry-board at 130 Hz. Interfacing of the animal from the dichroic cube was achieved with a low-autofluorescence patch cord (400 µm core diameter, 0.57 NA; MFP_400/430/3000-0.57_1m_FC-ZF1.25(F)_LAF, Doric Lenses), connected to the implanted cannula with a zirconia mating sleeve (SLEEVE_ZR_1.25; Doric Lenses), and covered with a black shrinking tube to minimize optical noise. For dual-site recordings, two of these systems were operated in parallel. Simultaneously, videographic images of the animal's eye were taken using a monochrome camera (DMK 33UX249; The Imaging Source) equipped with a macro objective (TMN 1.0/50; The Imaging Source) and a 780 nm long-pass filter (FGL780; Thorlabs), while the eye was illuminated at 850 nm with an infrared spotlight. Optogenetic stimulation was achieved with custom scripts written in MATLAB (v.R2019a, MathWorks), actuating on an NI-DAQ-card (USB-6001; National Instruments), controlling a 594 nm diode laser (Obis 594 nm LS 100 mW; Coherent). Laser light was coupled into the 580–680 nm port of the dichroic cube for activation of ChrimsonR in noradrenergic neurons of the LC. Measurements were synchronized by custom scripts written in MATLAB (MathWorks), actuating on an NI-DAQ card (PCIe-6323; National Instruments). For pharmacological experiments, data were first collected for the control condition, subsequently for the injection of saline (10 µl g^{-1} body-weight, i.p., ~15 min before the recording), and finally for the injection of desipramine (D3900-1G; Sigma Aldrich; 10 µg g^{-1} bodyweight, diluted in saline for injections of 10 µg g^{-1} bodyweight, i.p., ~15 min. before the recording), to avoid a bias in favor of the desipramine condition due to indicator bleaching. For experiments of LC lateralization, animals were anesthetized with isoflurane (1.5–2% in air) and placed on a heating pad to maintain body temperature. Recordings started 5–10 min after induction of anesthesia.

Data analysis for photometry and pupillometry recordings. For single-site photometry data, analysis of the raw photometry data was performed using a custom-written MATLAB script. First, to filter high frequency noise (above 1 Hz), the lowpass filter function was applied to both recorded signals: F560, F470/465 and control signal (Fcontrol, signal excited at either 405 nm or 415 nm).

Next, to correct for photobleaching of fluorescent signal, the baseline fluorescence Fcontrol$_{baseline}$ fit was calculated as a linear fit applied to the filtered Fcontrol, the F470/465 or the F560 signals during the baseline 5 s window preceding each stimulus. The signal of the NE indicators were expressed as a percentage change in fluorescence: $\Delta F/F_0 = 100 \times$ (F470/465/560(t) − Fcontrol$_{baseline}$ fit(t))/Fcontrol$_{baseline}$ fit(t), where F470/465/560(t) signifies the filtered fluorescence value at each time point t across the recording for either the 470 or 465 nm-excited signal or the 560 nm-excited signals, and Fcontrol$_{baseline}$ fit(t) denotes the value of the fitted control signal at the time point t. The final $\Delta F/F_0$ signal was averaged over the multiple trials and smoothed with a ten-point moving mean filter. In the case of optogenetic experiments, all traces were normalized to the pre-Yoh $\Delta F/F_0$ signal and plotted as percentage change.

For dual-site photometry data processing, the 405 and 470 nm-excited signals were fitted with a polynomial function of first to the fourth degree (based on visual inspection) using MATLAB's polyfit function, to capture the bleaching of each trace. Each signal was then divided by its fit, to correct for bleaching and normalize each signal. Traces were then smoothed with a moving-average filter (100 ms

window size). Finally, $\Delta F/F$ was calculated as the difference between the bleaching-corrected, normalized, smoothed signals excited at 405 and 470 nm (see Extended Data Fig. 7 for further details). To identify stimulus-evoked responses in pupillometric and photometry data, traces were cropped around each stimulation event, usually from 15 s before to 90 s after each event. Traces were then normalized by subtracting the median pupil diameter/fluorescence during the second before stimulus onset from each trace, before averaging all traces of a recording session. Finally, stimulus-evoked responses were defined as the median pupil diameter/fluorescence during the last second of stimulus presentation. Time constants of the decay of responses (τ_{off}) were estimated by an exponential fit starting at stimulus offset. Processing of pupillometric data was performed as described before[52]: briefly, the upper, lower, left and right edges of the pupil were tracked using DeepLabCut[53], samples with a certainty <0.5 were linearly interpolated between the next neighboring samples with a certainty of ≥0.5, and the pupil diameter was calculated as the maximum distance between two opposing points of the pupil. Eye opening was calculated by tracking the upper and lower edge of the eye, to remove blinking artefacts from pupil data by linearly interpolating regions in which the eye opening exceeds the moving median minus three times moving median absolute deviation with a sliding window of 30 s.

In vivo two-photon imaging

Two-photon imaging experiments during virtual navigation were carried out on a custom apparatus similar to that described in Curreli et al.[48]. nLightG signals were imaged using an Ultima Investigator scanhead (Bruker Corporation) equipped with galvo-resonant scanner, ×16/0.8 NA objective (Nikon), and multi-alkali photomultiplier tubes. Two-photon excitation was obtained using a Ti:Sapphire pulsed laser source tuned at 920 nm (Chameleon Ultra II, 80 MHz repetition rate, Coherent). Imaging average power at the objective focus was ~60–85 mW. Fluorescence emission was collected by a photomultiplier detector downstream of a bandpass filter (525/70 nm) and Detector output signal was first amplified and then digitalized at 12 bits. Imaging sessions were acquired using resonant-scanning at ~30 Hz and 3× optical zooming factor. Images contained 512 pixels × 512 pixels (pixel size, 0.53 µm).

A personalized virtual reality configuration was established by utilizing Blender, an open-source three-dimensional creation suite (v.2.78c) available at blender.org. The virtual setting consisted of a straight corridor with unidirectional movement (180 cm in length, 9 cm in width). The corridor's close-range walls exhibited three distinct white textures (vertical lines, mesh and circles) set against a black backdrop. The character's viewpoint encompassed a horizontal range of 220° and a vertical range of 80°, which was presented through a setup of five thin-bezel LED screens arranged in a composite tiling fashion. The animal's motion within the virtual corridor was simulated in a 1:1 ratio using a specially designed three-dimensional printed wheel (8 cm radius, 9 cm width) coupled with an optical rotary encoder (Avago AEDB-9140-A14, Broadcom Inc.). To capture the rotary encoder signals, a single board microcontroller (Arduino Uno R3, Arduino) was employed and the signals were subsequently converted into USB-HID-compliant serial mouse input. To provide water rewards (approximately 4 µl), a custom lick-port controlled by a solenoid valve (00431960, Christian Bürkert GmbH & Co.) was utilized, while lick responses were monitored using a capacitive indicator (MTCH102, Microchip Technology Inc.). The virtual reality rendering and two-photon imaging acquisition operated independently on asynchronous clocks, with synchronization between imaging acquisitions and behavior achieved through the utilization of the Ultima Investigator control system's start-of-frame transistor-transistor logic signal.

Two weeks after surgery, animals underwent water-scheduling, receiving approximately 1 ml of water per day. Weight was monitored daily, and it remained within 80–90% of the prescheduling weight

throughout all procedures. Mice were first habituated to the operator and to the experimental rig for two sessions of few minutes duration. Animals were then habituated to head-tethering while receiving water rewards upon spontaneous running bouts. Head-tethering time was progressively increased reaching 45 min in five sessions. On average, mice underwent eight training sessions where they were allowed to run spontaneously while receiving water rewards at pseudorandom times. Two-photon imaging experiments started on recording day 1, when mice were exposed to the virtual corridor for the first time and lasted for five consecutive days (days 1–5). Water rewards were available only at specific spatial locations in the virtual corridor. On recording days 1 and 2, the water reward was located at 85 cm from the beginning of the virtual corridor. At half of the recording session of day 3, the water reward was moved to a different position (145 cm) and was kept in that new position for recordings performed on days 4–5. In each virtual corridor crossing, the mouse was teleported to the beginning of the corridor after reaching the end of the track (intertrial timeout interval 5 s). If the mouse did not reach the end of the corridor within 120 s, the trial was automatically terminated, and the mouse was teleported to the beginning of the corridor after an intertrial timeout. On recording day 1, a set of reference images spanning different depths within the hippocampus was collected to identify an optical FOV and perform longitudinal imaging of the same population of CA1 neurons across experimental days 1–5. On each experimental session, three temporal series (12,500 frames per series; t-series duration, ~415 s), interleaved by 3-min breaks, were acquired during a virtual navigation session of ~45 min. At the end of each imaging session, animals were returned to their home cage.

Data analysis for two-photon imaging experiments. Analysis was performed using custom code written in Python v.3.6. t-series were preprocessed to correct motion artifacts using an open-source implementation of upsampled phase cross-correlation[54,55]. Motion correction was first carried out for each day of recording, where each t-series was motion corrected using its average projection as reference frame. Average temporal projections of corrected t-series were then combined in an image stack and used to compute x–y drifts with respect to the first element of the image stack. Computed x–y drifts were applied to the corrected t-series, which were then concatenated in a single movie containing all imaging frames of an experimental session. The resulting movie was finally motion corrected using the global temporal average projection as a reference image. To maximize the alignment across longitudinal experimental sessions, we used the results of within-session motion-correction procedures. For each session, we computed a global temporal average projection. Average projections were then combined in an image stack and subject to motion-correction procedure using the average projection of the image stack as reference. This procedure yielded an array of across-session x–y drifts, and a stack of motion-corrected average projections aligning each FOV across days. The resulting stack was used to compute a global average projection. The resulting x–y drifts were applied to all the frames of the relative imaging session, which was further motion corrected using the latest global average projection as a reference.

Fluorescence signals were computed either over the whole FOV as the average fluorescence intensity for each frame (Fig. 4a–i) or on identified ROIs (Fig. 4j–o). To identify potential axial displacement, for each session we computed the structural similarity index[56] of each frame with the average projection of the whole session. To minimize the impact of this residual uncorrected motion artifacts, frames with a structural similarity index <0.9 were excluded throughout all the following analysis. Importantly, the temporal dynamics of structural similarity values provide an internal control for the potential occurrence of stereotyped motion artifacts, which would appear as repeated events in the temporal dynamics of structural similarity.

Fluorescence signals from ROIs (putative CA1 cells) were computed using CITE-On[30] for both ROI detection and trace extraction. The CITE-On algorithm was executed setting detection confidence threshold to 0.05 and upscaling factor to 1. Within detected ROIs, functional nLightG signals were extracted from pixels with intensity comprised within the 50th and the 95th percentile of the distribution of fluorescence intensity. For each session, putative running epochs onset were identified as timepoints in which the mouse speed exceeded 1 cm s^{-1}. Runs were then selected when putative running epochs onsets were preceded by 2 s of immobility (average speed <1 cm s^{-1}) and followed by 5 s of sustained locomotion (average speed >1 cm s^{-1}). Reward epochs were selected using the time-stamp of reward delivery provided by the virtual reality software. For both running- and reward-event-triggered analysis, fluorescence signals were analyzed within each epoch defining a time window of (−2, 5) seconds relative to the epoch onset. For whole FOV and ROI analysis, fluorescence F_0 was defined as the average raw fluorescence intensity value observed in the interval (−2,0) seconds preceding the epoch onset. Within each epoch of (−2, 5) seconds fluorescence values $F(t)$ were computed filtering raw traces with a uniform mean filter (width 500 ms) centered at t, and $\Delta F/F_0$ was calculated as $(F(t) − F_0)/F_0$. The shuffled traces reported in Extended Data Figs. 8 and 9 were computed as the average of 1,000 shuffling of the raw fluorescence traces with respect to behavioral event (either beginning of running or crossing the reward position). Least-squares linear models were fitted on each individual session for each animal using data recorded within event-triggered epochs intervals. Model fitting was performed using ordinary least-squares implementation in SciPy (v.1.10.1)[57]. For running epochs data were selected within (0,5) seconds, while for reward epochs within (0,3) seconds. Average models were computed as averages of models fitted on individual animals' data.

Pairwise correlation analysis of ROI signals was conducted measuring the Pearson's product-moment correlation coefficient for pairs of ROIs using data from the intervals (0,5) seconds or (0,3) seconds for running and reward epochs, respectively. Self-correlations were removed. Hierarchical clustering of correlation matrices was performed using the agglomerative unweighted pair group method with arithmetic mean algorithm implemented in SciPy[57] over the Euclidean distance.

Immunohistochemistry

For transcardial perfusions, mice were deeply anesthetized with intraperitoneal injections of Ketamine/Xylazine in saline (180/24 mg kg^{-1}), and deep anesthesia was confirmed by absence of the hind paw withdrawal reflex. Mice were initially perfused with ~50 ml of PBS, and subsequently with ~50 ml of paraformaldehyde (PFA) (4% in PBS). Explanted brains were postfixed in 4% PFA for at least 24 h, embedded in 3% agarose and coronal slices of ~50 μm thickness were obtained with a vibratome (VT100S; Leica Biosystems). Unspecific antibody binding sites in brain slices were blocked (10% normal goat serum (NGS) and 0.3% Triton X-100 in PBS, 2 h, room temperature), before slices were incubated with primary antibodies against eGFP (chicken a-GFP, 1:750; catalog no. A10262, ThermoFisher Scientific) and tyrosine hydroxylase (LC only; rabbit a-TH, 1:1,000; catalog no. AB152, Merck Millipore) in carrier solution (2% NGS and 0.3% Triton X-100 in PBS, 48 h, 4 °C). Slices were then washed in PBS (three times for 5 min) before incubation with secondary antibodies (Alexa Fluor 488 goat anti-chicken; catalog no. A11039, ThermoFisher Scientific, and Alexa Fluor 647 goat anti-rabbit; catalog no. A32733, ThermoFisher Scientific; both diluted 1:1,000 in carrier solution) overnight at 4 °C. Finally, slices were again washed in PBS (three times for 5 min), incubated in 4,6-diamidino-2-phenylindole in PBS for 5–10 min and mounted on microscope slides using Fluoromount (Serva). Slices were then imaged using an epifluorescence microscope (AxioObserver, Zeiss) with a ×20/0.8 NA air objective and images were processed using ImageJ v.1.52 (Fiji)[45].

Statistical analyses

For in vitro analysis of indicator variants, the statistical significance of their responses was determined using GraphPad Prism v.9.0.0 on a case-by-case basis using either a two-tailed unpaired Student's t-test with Welch's correction or a Brown-Forsythe analysis of variance (ANOVA) test followed by Dunnett's T3 multiple comparison. For in vivo single-site photometry experiments, we used one-sample, paired and unpaired t-tests for statistical analysis of parametric data, while Wilcoxon rank-sum or signed-rank tests for analysis of nonparametric data. For in vivo dual-site photometry experiments, one- and two-sample, two-tailed t-tests were performed to compare a single sample against a reference value or two samples against each other, after normality of the data was confirmed using a Jarque–Bera test. For comparison of three or more groups, one-way ANOVA was performed and—when significant—post hoc comparisons between groups were performed using Tukey's test. All P values are indicated in the figure legends. Data are displayed as mean with s.e.m. or s.d., as noted in the figure legends. No statistical methods were used to predetermine sample size.

Reporting summary

Further information on research design is available in the Nature Portfolio Reporting Summary linked to this article.

Data availability

DNA and protein sequences for indicators developed in this study were deposited on NCBI (accession numbers ON737776–ON737782) or are available in Supplementary Data 1 of Supplementary Information. DNA plasmids used for viral production have been deposited both with the UZH Viral Vector Facility (https://vvf.ethz.ch/) and on AddGene. Viral vectors can be obtained either from the Patriarchi laboratory, the UZH-VVF or AddGene. Source data are provided with this paper. Due to its large size raw data can be made available only upon reasonable request.

Code availability

Custom MATLAB code is available on https://github.com/patriarchilab/nLightG under a GNU v.3 license.

References

41. Wan, Q. et al. Mini G protein probes for active G protein–coupled receptors (GPCRs) in live cells. *J. Biol. Chem.* **293**, 7466–7473 (2018).
42. Laschet, C., Dupuis, N. & Hanson, J. A dynamic and screening-compatible nanoluciferase-based complementation assay enables profiling of individual GPCR–G protein interactions. *J. Biol. Chem.* **294**, 4079–4090 (2019).
43. Pollok, S. & Reiner, A. Subunit-selective iGluR antagonists can potentiate heteromeric receptor responses by blocking desensitization. *Proc. Natl Acad. Sci. USA* **117**, 25851–25858 (2020).
44. Edelstein, A. D. et al. Advanced methods of microscope control using μManager software. *J. Biol. Methods* **1**, e10 (2014).
45. Schindelin, J. et al. Fiji: an open-source platform for biological-image analysis. *Nat. Methods* **9**, 676–682 (2012).
46. Tillage, R. P. et al. Elimination of galanin synthesis in noradrenergic neurons reduces galanin in select brain areas and promotes active coping behaviors. *Brain Struct. Funct.* **225**, 785–803 (2020).
47. Parlato, R., Otto, C., Begus, Y., Stotz, S. & Schütz, G. Specific ablation of the transcription factor CREB in sympathetic neurons surprisingly protects against developmentally regulated apoptosis. *Development* **134**, 1663–1670 (2007).
48. Curreli, S., Bonato, J., Romanzi, S., Panzeri, S. & Fellin, T. Complementary encoding of spatial information in hippocampal astrocytes. *PLoS Biol.* **20**, e3001530 (2022).
49. Dombeck, D. A., Harvey, C. D., Tian, L., Looger, L. L. & Tank, D. W. Functional imaging of hippocampal place cells at cellular resolution during virtual navigation. *Nat. Neurosci.* **13**, 1433–1440 (2010).
50. Sheffield, M. E. J. & Dombeck, D. A. Calcium transient prevalence across the dendritic arbour predicts place field properties. *Nature* **517**, 200–204 (2015).
51. Akam, T. & Walton, M. E. pyPhotometry: open source Python based hardware and software for fiber photometry data acquisition. *Sci. Rep.* **9**, 3521 (2019).
52. Yang, W. et al. Anesthetics fragment hippocampal network activity, alter spine dynamics, and affect memory consolidation. *PLoS Biol.* **19**, e3001146 (2021).
53. Mathis, A. et al. DeepLabCut: markerless pose estimation of user-defined body parts with deep learning. *Nat. Neurosci.* **21**, 1281–1289 (2018).
54. Guizar-Sicairos, M., Thurman, S. T. & Fienup, J. R. Efficient subpixel image registration algorithms. *Opt. Lett.* **33**, 156–158 (2008).
55. van der Walt, S. et al. scikit-image: image processing in Python. *PeerJ* **2**, e453 (2014).
56. Avanaki, A. N. Exact global histogram specification optimized for structural similarity. *Opt. Rev.* **16**, 613–621 (2009).
57. Virtanen, P. et al. SciPy 1.0: fundamental algorithms for scientific computing in Python. *Nat. Methods* **17**, 261–272 (2020).

Author contributions

T.P. led the study. T.P., V.R. and C.K. conceived the sensor engineering strategy. Z.K., V.R. and C.K. performed molecular cloning, in vitro indicator screening and characterization in HEK293T cells and neurons, and analyzed data under the supervision of T.P. J.D. measured two-photon brightness under the supervision of L.R., B.W. and T.P. T.Z., A.R., L.M.W. and L.S. performed and T.Z. and A.R. analyzed patch-clamp fluorometry experiments. M.A.B. prepared cortical neuronal cultures under the supervision of D.B. Z.K., M.W. and M.H. performed and analyzed imaging experiments in acute brain slices under the supervision of T.P. Z.K., M.W. and M.H. performed and analyzed in vivo tail-lift experiments under the supervision of T.P. S.N.D. and M.W. performed and analyzed optogenetic experiments

Competing interests

Additional information

Extended Data Fig. 1 | See next page for caption.

Extended Data Fig. 1 | Development of nLightG and nLightR. a, Representative images of indicators expressed in HEK293T cells in the absence or presence of NE (10 μM) and heatmaps of fluorescence responses. Scale bar, 15 μm. **b**, Quantification of basal brightness and dynamic range. n = 21 cells. **c, d**, Normalized fluorescence intensity dose-response curves of nLightG and nLightR for NE (**c**) and DA (**d**) in HEK293T cells. Four-parameter dose-response curve fits determined the EC_{50} values. n = 3 wells per concentration for each ligand. **e**, Sequence of RdLight1, dLight1.3b and sperm whale Alpha-1 AR with reference BW numbering. **f, g**, Dynamic range of red (**f**) or green (**g**) indicator variants generated by grafting at different BW registries. The response was measured in HEK293T cells upon addition of NE (10 μM). n = 21 cells. P values were as follows: 1.585×10^{-8} (**f**); 5.66–6.30, 4.149×10^{-17}; 5.65–6.31, 9.093×10^{-7}; 5.64–6.32,

2.199×10^{-8}; 5.62–6.34, 4.341×10^{-14}; 5.61–6.35, 3.283×10^{-14} (**g**). **h**, Dynamic range of the red indicator variants with or without ICL2 grafting measured in HEK293T cells. n = 21 cells. $P = 2.625 \times 10^{-5}$. **i**, Left, time trace of the relative fluorescent response of nLightR (with or without ICL2 graft). Saturating concentrations of DA (200 μM) and NE (10 μM) were added consecutively. n = 21 cells for each trace. Right, ratio of average fluorescent responses to DA versus NE from traces shown on left. $P = 2.292 \times 10^{-4}$. **j**, Same as in (**h**) but for nLightG and using the ICL2 of dLight1.3b for grafting. P = 0.566. **k**, Same as in (**i**) but for nLightG. $P = 2.103 \times 10^{-3}$. All data are shown as mean ± SEM. All experiments were repeated at least three times with similar results. Mean values were compared using a two-tailed Students t-test with Welch's correction.
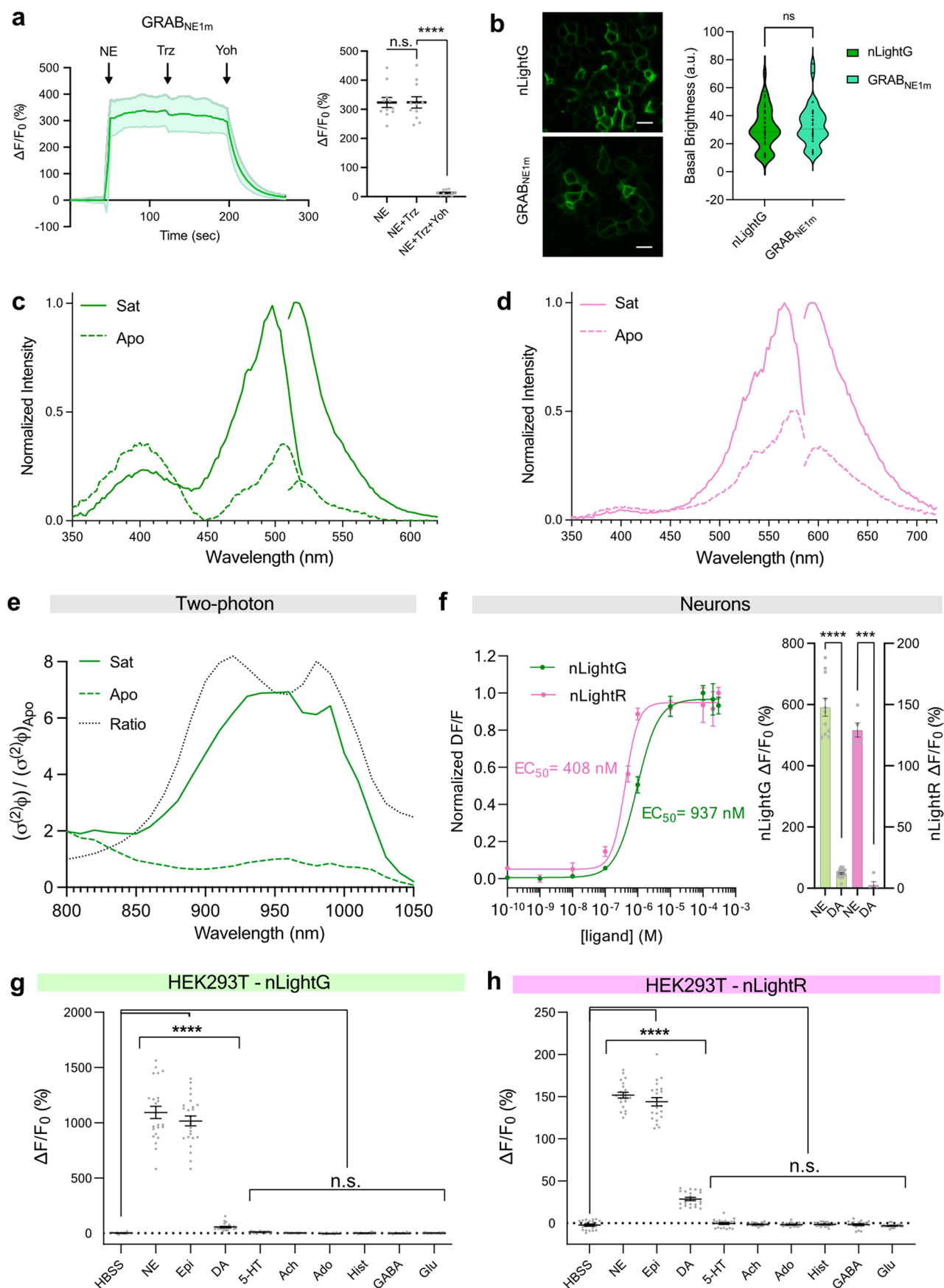
Extended Data Fig. 2 | See next page for caption.

Extended Data Fig. 2 | Additional in vitro characterization of nLightG and nLightR. a, Fluorescence response of GRAB$_{NE1m}$ in HEK293T, and quantification of mean responses to ligands. NE (10 µM), trazodone (Trz, 100 nM) and (Yoh (100 nM) were added consecutively. Error bars represent mean ± SEM. n = 11 cells from 3 independent experiments. n.s., P = 0.9902; **** P = 1.374×10^{-8}. **b**, Left, representative images of cellular brightness for nLightG and GRAB$_{NE1m}$. Scale bars, 20 µm. Right, violin plot comparison of basal brightness between nLightG and GRAB$_{NE1m}$. Medians are thin dotted lines. n = 46, 37 cells for nLightG and GRAB$_{NE1m}$, respectively, from 3 independent experiments. n.s., not significant. P = 0.4839. **a-b**, Two-tailed Students t-test with Welch's correction. **c**, One-photon fluorescence excitation and emission spectra of nLightG in the presence (Sat) or absence (Apo) of NE (100 µM). n = 4 wells. **d**, same as in (**c**) for nLightR. **e**, Two-photon brightness of nLightG in HEK cells. Spectra are normalized to the Apo form at 950 nm. Ratio between Sat and Apo is shown as black dotted line. n = 3 dishes. **f**, Left, normalized fluorescence dose-response curves of NE in nLightG- and nLightR-expressing neurons. Datapoints were fitted with four-parameter

dose-response curves to determine EC$_{50}$ values. n = 11 cells for nLightG and n = 3 cells for nLightR from three independent experiments. Right, maximal ΔF/F$_0$ response of nLightG- and nLightR-expressing neurons to NE or DA. Both ligands were separately applied at 300 µM concentration on the cells. n = 11, 24 cells for nLightG with NE and DA, respectively, and n = 5 cells for nLightR with NE or DA. Two-tailed Students t-test with Welch's correction. P values: 3.421×10^{-9}, nLightG; 2.240×10^{-6}, nLightR. mean ± SEM. **g**, Fluorescence response of nLightG to non-ligand neurotransmitters (10 µM). Welch ANOVA with Dunett's multiple comparison test. Data are shown as mean ± SEM. n (cells) as follows: 12 for HBSS; 23 for NE; 24 for Epi; 23 for DA; 23 for 5-HT; 26 for Ach; 23 for Ado; 21 for Hist; 22 for GABA; 21 for Glu. P values: NE, P < 10^{-14}; Epi, P < 10^{-14}; DA, P = 0.931×10^{-6}; Ser, P = 0.066; Ach, P = 0.999; Ado, P = 0.705; His, P = 0.999; GABA, P = 0.999; Glu, P = 0.999. **h**, same as in (**g**) for nLightR. P values: NE, P < 10^{-14}; Epi, P < 10^{-14}; DA, P < 10^{-14}; Ser, P = 0.887; Ach, P = 0.998; Ado, P = 0.999; His, P = 0.999; GABA, P = 0.999; Glu, P = 0.998. All experiments were repeated at least three times with similar results.
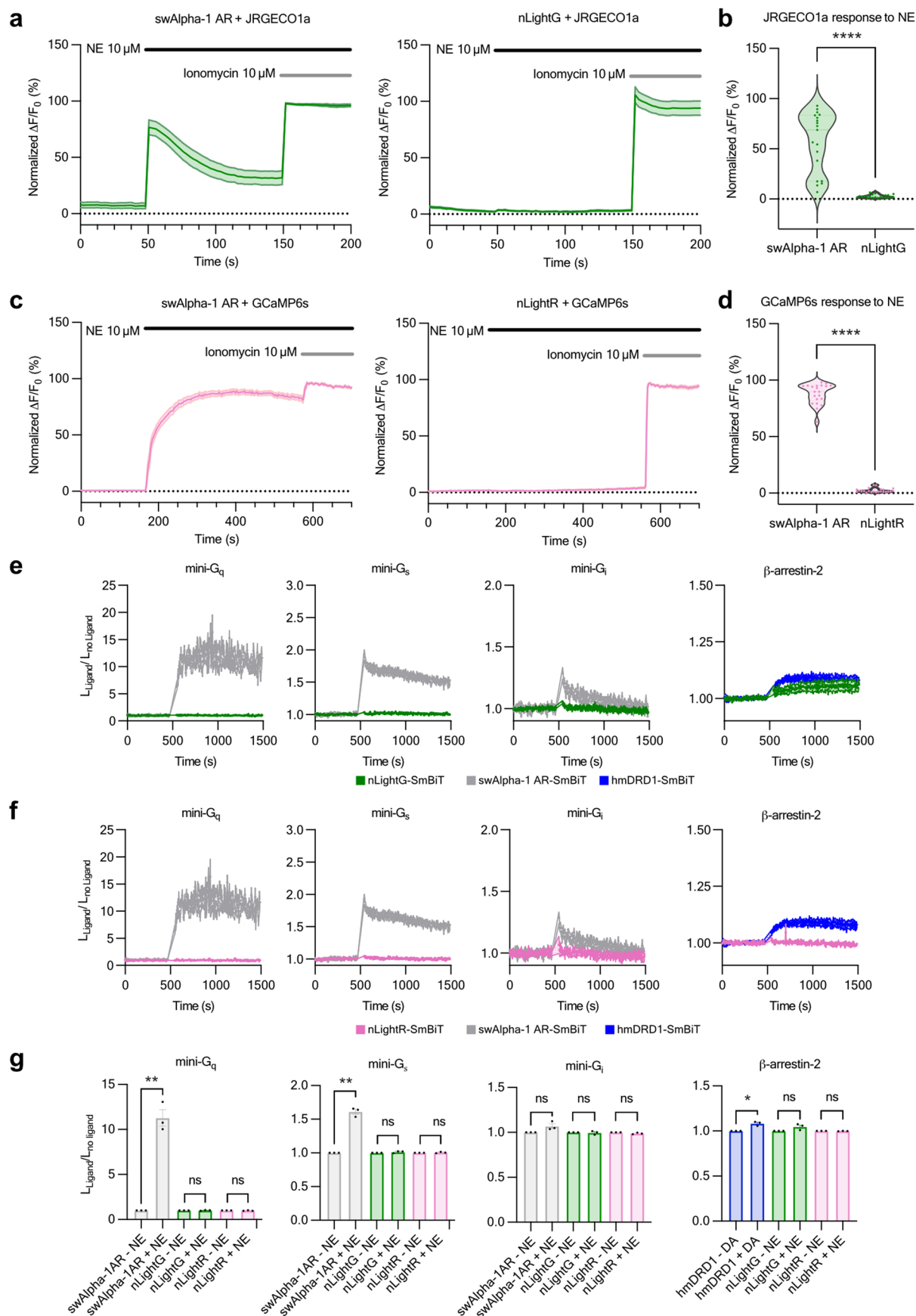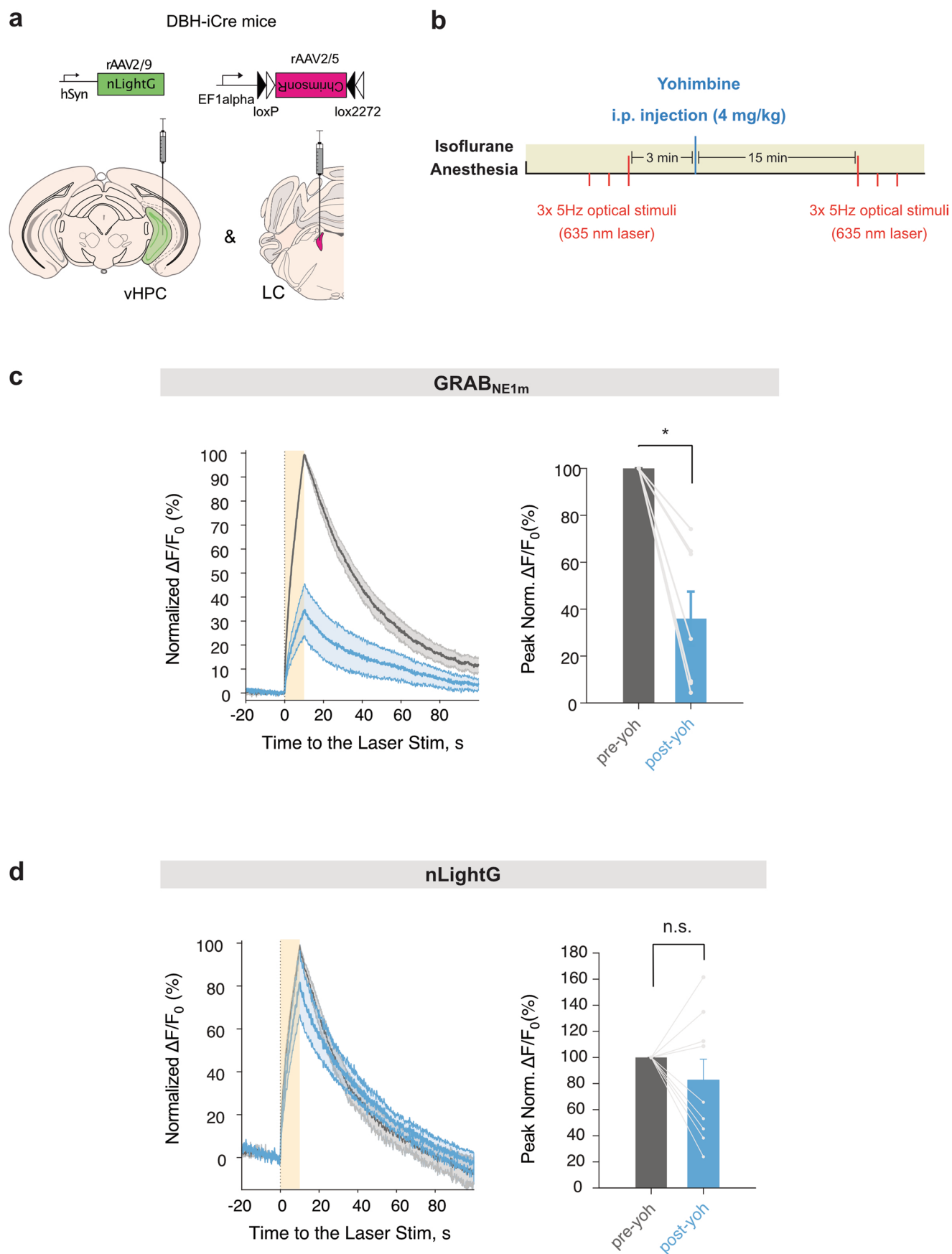
Extended Data Fig. 3 | See next page for caption.

Extended Data Fig. 3 | Signaling characterization of nLightG and nLightR. **a**, Intracellular calcium signaling for nLightG and swAlpha-1 AR. Calcium activity was measured at baseline conditions, during NE (10 μM) and ionomycin (10 μM). Signals were normalized to ionomycin response. n = 19 and 22 cells for swAlpha-1 AR-jRGECO1a and nLightG-jRGECO1a. **b**, Statistical analysis of **a**. Each data point is the mean jRGECO1a response for one cell. Violin plot represents the kernel density estimate of the probability density function for each sample. Two-tailed Students t-test with Welch's correction. P = 2.887×10^{-7}. **c**, Same as in **a** for nLightR. n = 21 and 23 cells for swAlpha-1 AR-GCaMP6s and nLightR-GCaMP6s, respectively. **d**, Same as in **b** for **c**. P = 3.393×10^{-21}. **e**, Luminescence signal ratios upon ligand stimulation (NE, 10 μM). The ratios were normalized to the baseline luminescence ratio before the addition of NE. Each trace is the average of three independent experiments. **f**, Same as in **e** but for nLightR. **g**, Statistical analysis of data shown in **e** and **f**. Two-tailed Students t-test with Welch's correction. P values were as follows: mini-Gq, swAlpha-1 AR, 7.75×10^{-3}; nLightG, 0.590; nLightR, 0.589; mini-Gs, swAlpha-1 AR, 3.88×10^{-3}; nLightG, 0.281; nLightR, 0.410; mini-Gi, swAlpha-1 AR, 0.126; nLightG, 0.792; nLightR, 0.147; β-arrestin-2, swAlpha-1 AR, 8.97×10^{-2}; nLightG, 0.134; nLightR, 0.377. All data are shown as mean ± SEM. All experiments were repeated three times with similar results.

**Extended Data Fig. 4 | See next page for caption.**

Extended Data Fig. 4 | Pharmacological characterization of nLightG and GRAB$_{NE1m}$ in anesthetized mice. a, Schematic representation of viral injections for photometry recordings of nLightG or GRAB$_{NE1m}$ in vHPC during optogenetic stimulation of LC in anesthetized mice. **b**, Experimental protocol for optogenetic stimulation combined with drug injection during isoflurane anaesthesia. **c**, Left, average traces of normalized signal changes ($\Delta F/F_0$ %) of GRAB$_{NE1m}$ photometry recordings in response to three LC optical stimulation protocols (5 Hz) pre- and post- yohimbine injection. Signals were normalized to the average peak value pre-yohimbine. The period of optogenetic stimulation is represented with an orange shade. Right, statistical comparison of peak normalized $\Delta F/F_0$ % responses to 5 Hz LC between pre- and post- yohimbine injection. P = 0.0014, n = 7 mice, two-sided one-sample t-test. **d**, Same as in **c** for nLightG. n.s., non-significant (P = 0.31), n = 9 mice, two-sided one-sample t-test. All data are shown as mean ± S.E.M.
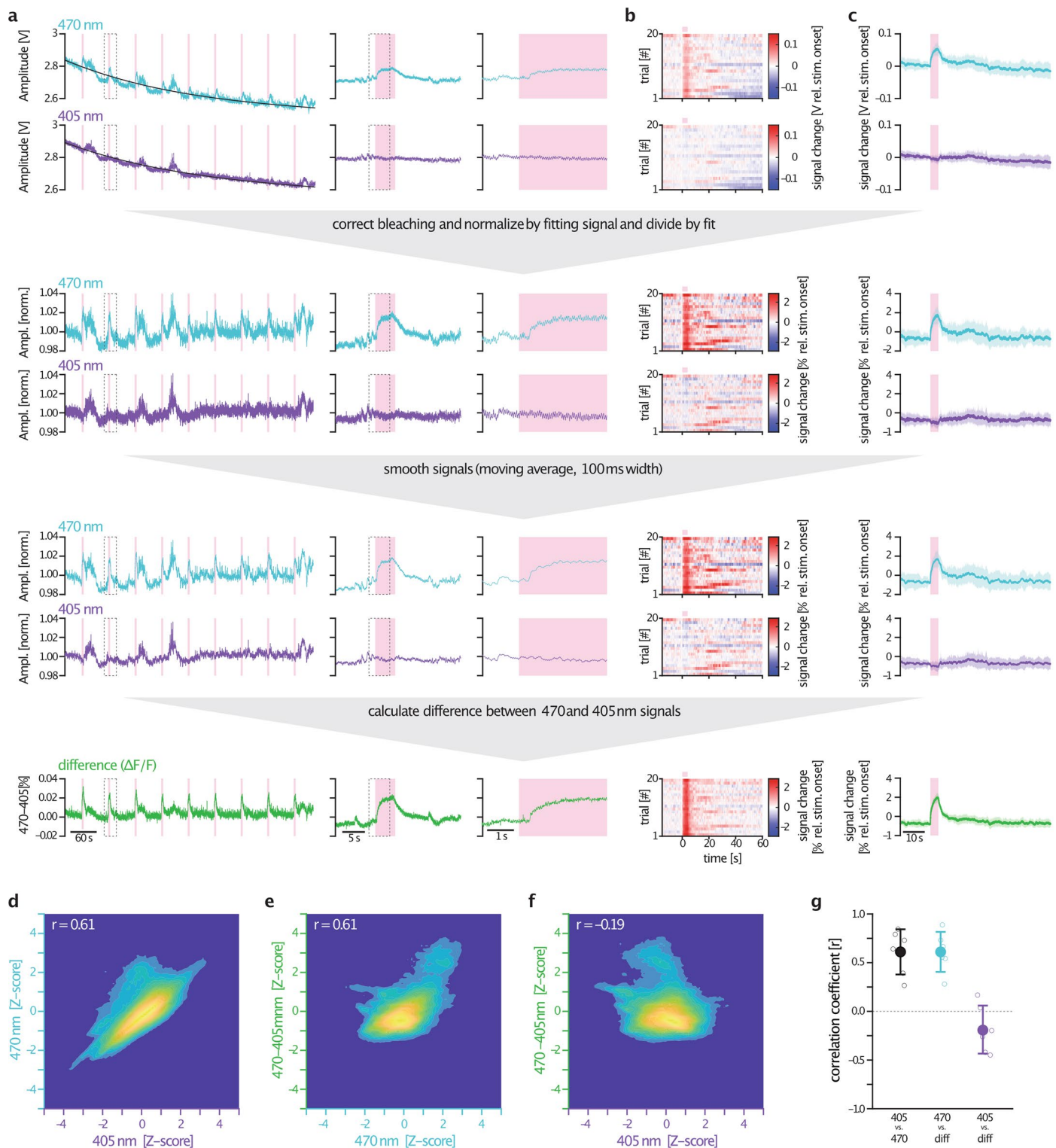
Extended Data Fig. 5 | Processing of fiber photometry data presented in Fig. 4. a, Processing of an example photometry trace in response to optogenetic stimulation (pink) of the same site (LC). nLightG was excited at wavelengths of 470/10 ('ligand-dependent') and 405/10 nm ('control'), in a temporally interleaved manner. 10 minutes-long, 30 seconds-long, and 5 seconds-long recordings are shown from left to right, dashed boxes indicate magnified regions. Firstly, a 1st-4th degree polynomial fit was applied (black line). Subsequently, signals were divided by this fit, to correct for bleaching and normalize them (center top). Next, signals were smoothed with a moving-average filter of a 100 ms (center bottom). Finally, $\Delta F/F_0$ was calculated as the difference between the resulting signals excited at 470/10 and 405/10 nm (bottom). Original signals contained substantial artefacts likely to originate from locomotion and hemodynamics (as seen by the oscillations of 10–13 Hz likely to originate from the animal's heartbeat[37] in the bleaching-corrected unsmoothed trace). These artefacts are substantially reduced by subtracting the 405/10 nm-excited signal from the 470/10 nm-excited signal. **b**, Heatmap of 20 individual trials of optogenetic stimulation, corresponding to the processing steps shown in **a**. **c**, Mean ± standard deviation of the trials shown in **b**. **d**, Plot correlating z-scored data across all animals (n = 6) excited at 405/10 nm vs 470/10 nm (Pearson's correlation coefficient r = 0.61). **e/f**, Plot correlating z-scored data across all animals (n = 6) excited at 470/10 nm **e** and 405/10 nm **f** against the calculated $\Delta F/F_0$ (**e**, Pearson's correlation coefficient r = 0.61; **f**, Pearson's correlation coefficient r = −0.19). **g**, Individual Pearson's correlation coefficients from **d,e,f** (n = 6 animals). Data are shown as mean ± standard deviation.
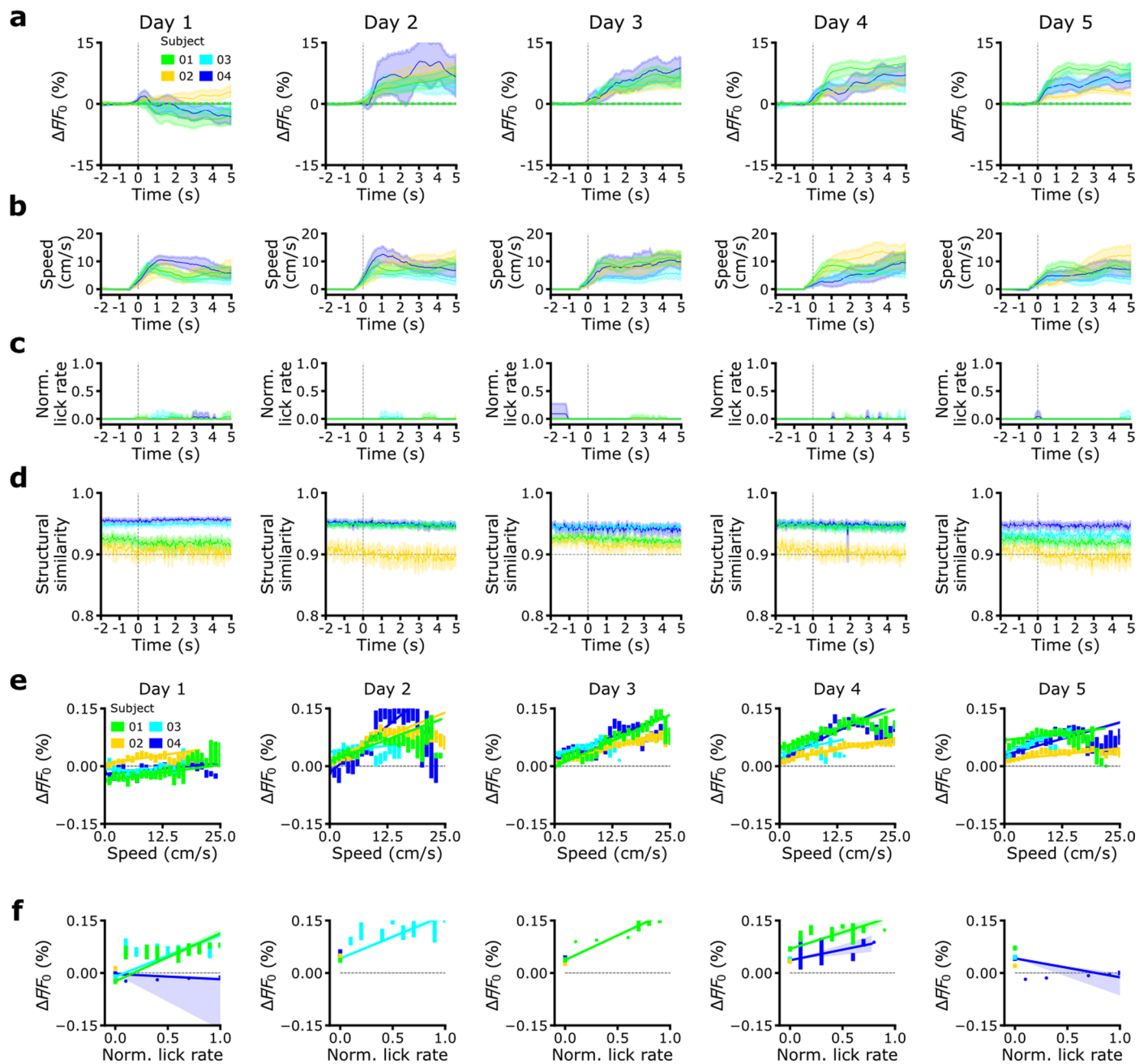
Extended Data Fig. 6 | Running-induced nLightG signals in the mouse hippocampus. a, Event-triggered averages for individual animals (n = 4) showing the changes in nLightG signal amplitude over the whole field-of-view when the mouse started running for the five consecutive recording days. Signals were recorded using two-photon microscopy. The colors indicate the different animals (subject 1–4). **b**, Event-triggered averages of running speed of individual animals in the virtual corridor when the mouse started running. Color code as in **a**. **c**, Same as in **b** for lick rate. **d**, Structural similarity in the time interval displayed in **a**–**c**. **e**, nLightG signal amplitude as a function of running speed for individual animals. **f**, nLightG signal amplitude as a function of lick rate for individual animals. In **a** to **f**, data is presented as (mean ± 95% confidence interval).
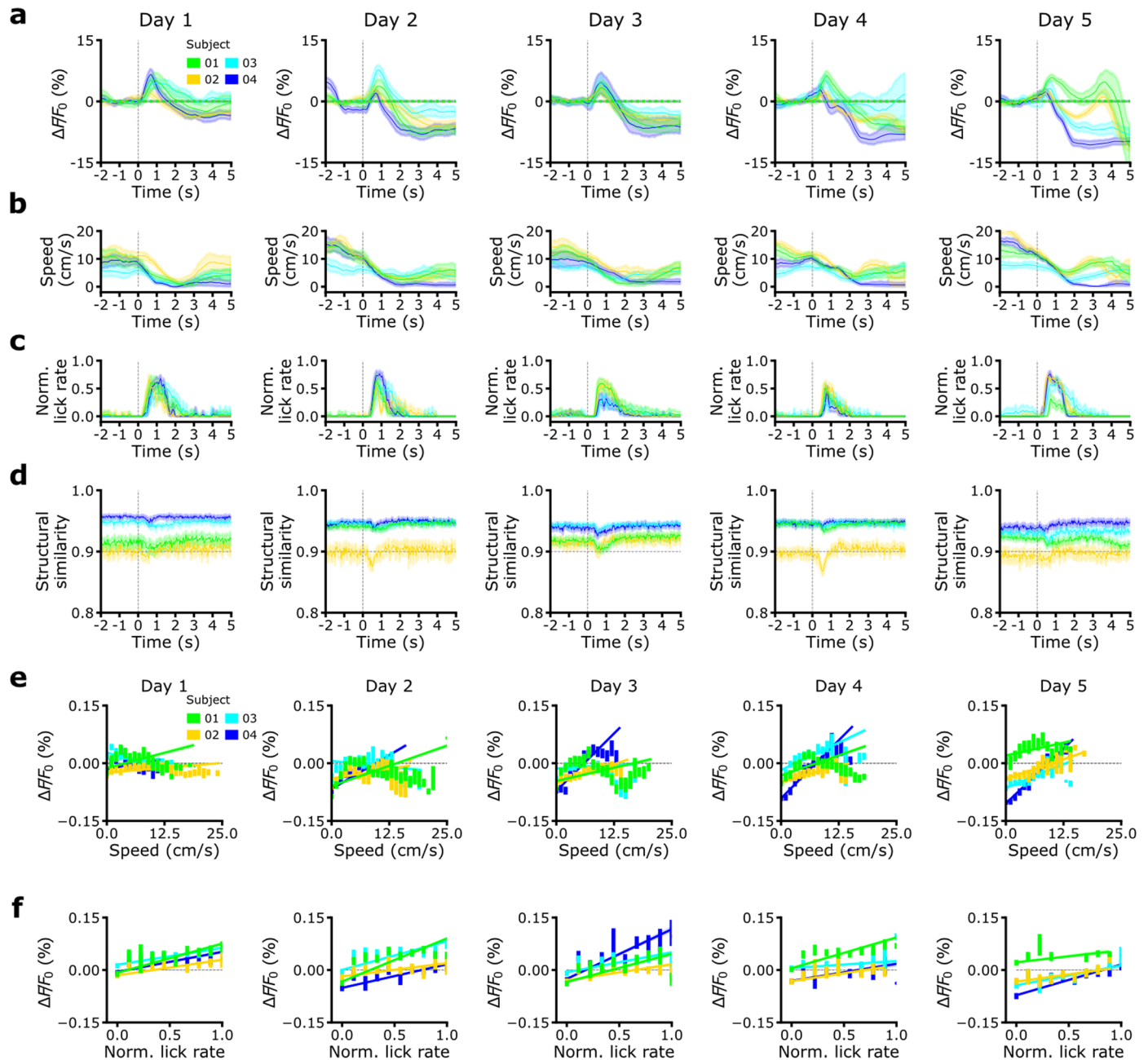
Extended Data Fig. 7 | nLightG signals associated with reward position in the mouse hippocampus. a, Event-triggered averages for individual animals (n = 4) showing the changes in nLightG signal amplitude over the whole field-of-view when the mouse crossed the reward position for the five consecutive days of recording. Signals were recorded using two-photon microscopy. The colors indicate the different animals (subject 1–4). **b**, Event-triggered averages

of running speed of individual animals in the virtual corridor when the mouse crossed the reward position. Color code as in **a**. **c**, Same as in **b** for lick rate. **d**, Structural similarity in the time interval displayed in **a–c**. **e**, nLightG signal amplitude as a function of running speed for individual animals. **f**, nLightG signal amplitude as a function of lick rate for individual animals. In **a** to **f**, data is presented as (mean ± 95% confidence interval).
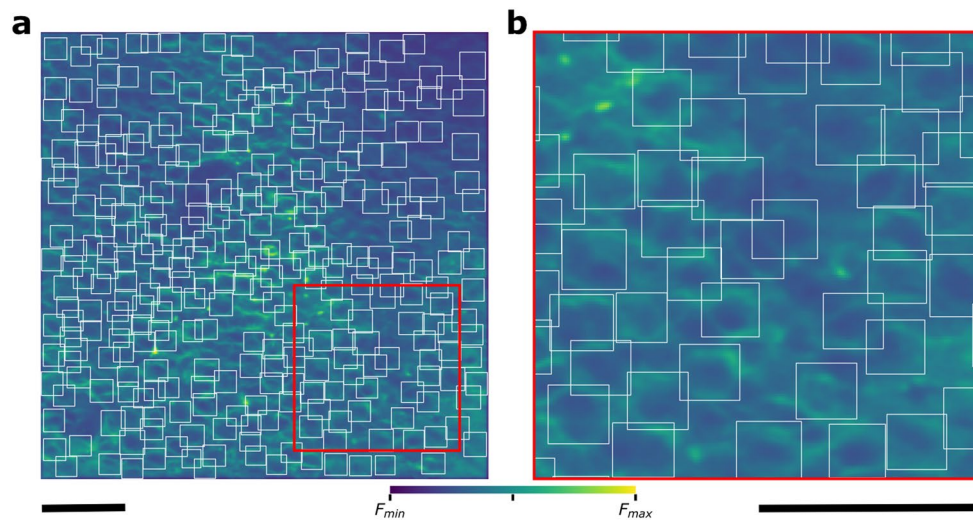
Extended Data Fig. 8 | ROI selection for analysis of in vivo two-photon data.
a-b, Representative field-of-view showing hippocampal CA1 neurons expressing nLightG in vivo (same field-of-view as in Fig. 4j). The red solid line in (a) indicates the zoomed in area shown in (b). White boxes indicate regions-of-interest (ROIs) identified within the field-of-view and centered on putative cells using the machine learning algorithm CITE-On[30]. Scale bar, 50 μm.
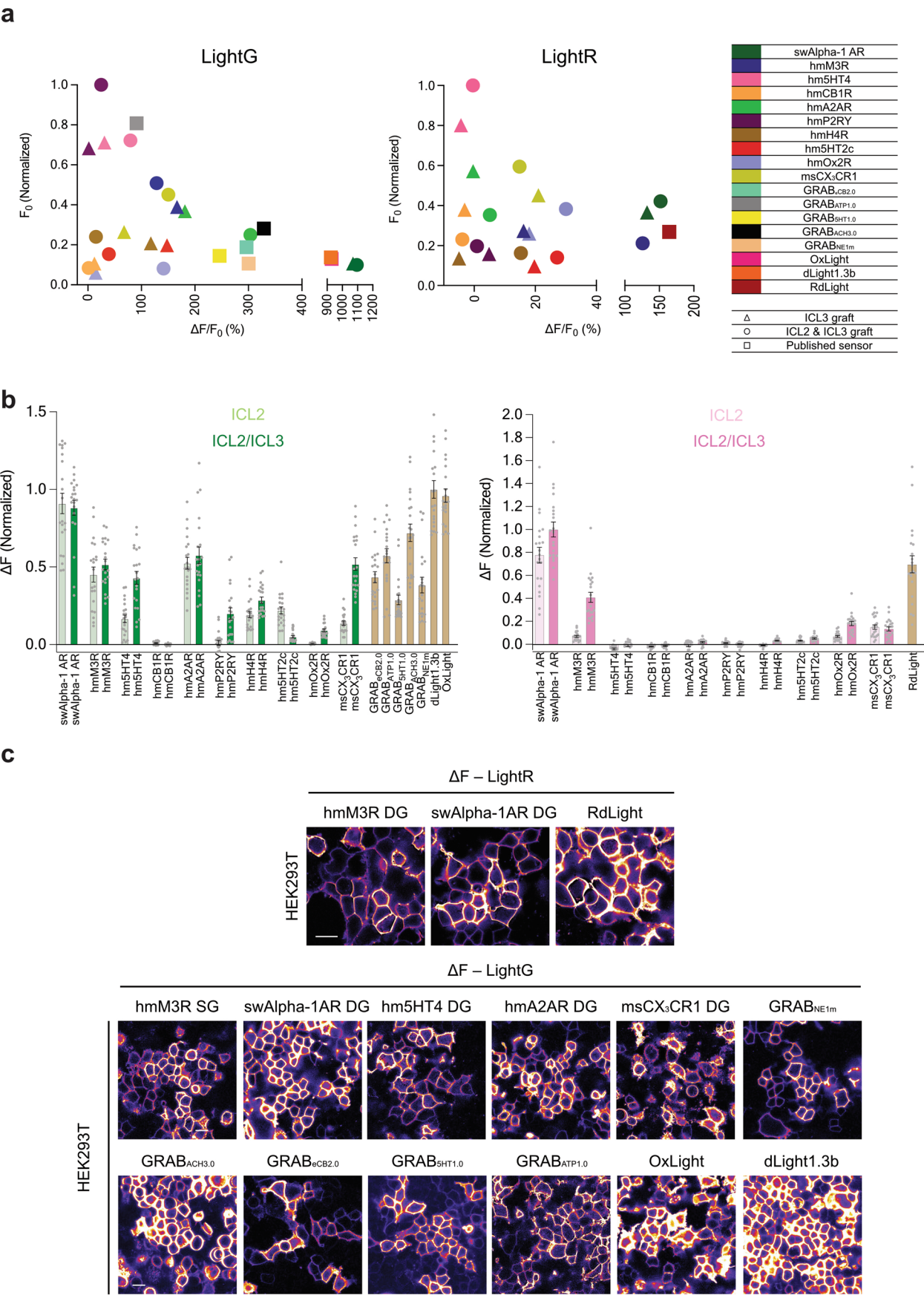
Extended Data Fig. 9 | See next page for caption.

Extended Data Fig. 9 | Further comparison between our and published indicators. a, Basal brightness of LightG and LightR indicator constructs plotted against their fluorescence response $\Delta F/F_0$ in HEK293T cells. Basal brightness values reflect the average brightness of indicator-expressing HEK293T cells in the ligand-free state. Grafts containing only the ICL3 module of LightG or LightR are represented as triangles. Grafts containing ICL2 and ICL3 modules of LightG or LightR are represented as circles. Previously published indicators are represented as rectangles. **b**, Absolute changes in fluorescence (ΔF) of LightG (green) and LightR (red) grafts measured in HEK293T cells for a set of ten GPCRs. n = 21 cells from three independent experiments. Data were obtained from the same imaging experiments shown in Fig. 5. **c**, Heatmap of ΔF for a subset of indicators (those with $\Delta F > 0.3$). Scale bars, 20 μm. All experiments were repeated at least three times with similar results.
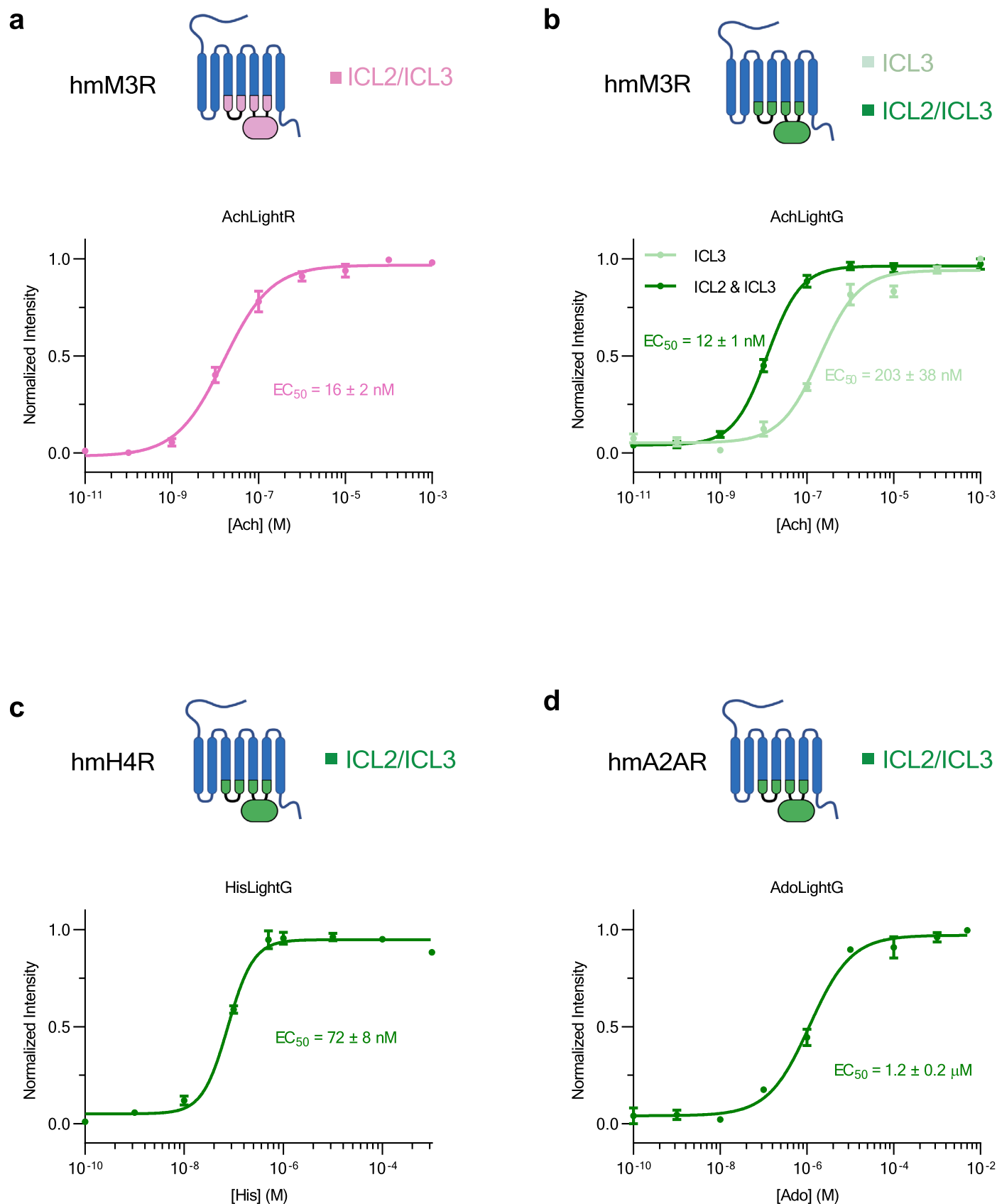
Extended Data Fig. 10 | Ligand EC$_{50}$ measurements for a subset of indicators. Normalized fluorescence dose-response curves of **a**, AchLightR (AchLightR-DG, hmM3R double graft); **b**, AchLightG (AchLightG-SG, hmM3R single graft, light green; AchLightG-DG, double graft, dark green); **c**, HisLightG (hmH4R, double-graft); and **d**, AdoLightG (hmA2AR, double-graft). All sensors were expressed in HEK293T cells and titrated with their endogenous agonists. Datapoints were fitted with four-parameter dose-response curves to determine the EC$_{50}$ values. n = 3 wells per concentration for each ligand. All data are shown as mean ± SEM and all experiments were repeated three times with similar results.

Corresponding author(s): Tommaso Patriarchi

Last updated by author(s): 05/22/2023

Reporting Summary

Nature Research wishes to improve the reproducibility of the work that we publish. This form provides structure for consistency and transparency in reporting. For further information on Nature Research policies, see our Editorial Policies and the Editorial Policy Checklist.

Statistics

For all statistical analyses, confirm that the following items are present in the figure legend, table legend, main text, or Methods section.

n/a	Confirmed	
☐	☒	The exact sample size (n) for each experimental group/condition, given as a discrete number and unit of measurement
☐	☒	A statement on whether measurements were taken from distinct samples or whether the same sample was measured repeatedly
☐	☒	The statistical test(s) used AND whether they are one- or two-sided *Only common tests should be described solely by name; describe more complex techniques in the Methods section.*
☒	☐	A description of all covariates tested
☐	☒	A description of any assumptions or corrections, such as tests of normality and adjustment for multiple comparisons
☐	☒	A full description of the statistical parameters including central tendency (e.g. means) or other basic estimates (e.g. regression coefficient) AND variation (e.g. standard deviation) or associated estimates of uncertainty (e.g. confidence intervals)
☐	☒	For null hypothesis testing, the test statistic (e.g. F, t, r) with confidence intervals, effect sizes, degrees of freedom and P value noted *Give P values as exact values whenever suitable.*
☒	☐	For Bayesian analysis, information on the choice of priors and Markov chain Monte Carlo settings
☒	☐	For hierarchical and complex designs, identification of the appropriate level for tests and full reporting of outcomes
☐	☒	Estimates of effect sizes (e.g. Cohen's d, Pearson's r), indicating how they were calculated

Our web collection on statistics for biologists contains articles on many of the points above.

Software and code

Policy information about availability of computer code

Data collection

Below is the software used for data collection in this manuscript:
- Zeiss Zen, Zen Blue (https:/ /www.zeiss.com/microscopy/int/products/microscope-software/zen-lite.html)
- Doric Neuroscience Studio v6.1.2.0 (https://neuro.doriclenses.com/products/doric-neuroscience-studio)
- MATLAB vR2019b (https://www.mathworks.com/products/matlab.html)
- Bonsai v2.6.2 (https://neurophotometrics.com/documentation)
- Blender, version 2.78c (https://blender.org)
- Python 3.6 (https://www.python.org)
- Arduino IDE (https://www.arduino.cc/)
- MicroManager2.0 (https://micro-manager.org/Download_Micro-Manager_Latest_Release)
- pClamp 10.7 (https://support.moleculardevices.com/s/article/Axon-pCLAMP-10-Electrophysiology-Data-Acquisition-Analysis-Software-Download-Page)
- ProFit 7.0 (https://quansoft.com/)

Data analysis

Below is the software used for data analysis in this manuscript:
- ImageJ v1.52 (http://imagej.nih.gov/ij/download.html)
- ProFit 7.0 (https://quansoft.com/)
- Python 3.6 (https://www.python.org/)
- SciPy v.1.10.1 (https://scipy.org/)
- GraphPad Prism v9.0.0 (https://www.graphpad.com/scientific-software/prism/)
- MATLAB versions R2019a, R2019b (https://www.mathworks.com/products/matlab.html)
Custom MATLAB code is available on https://github.com/patriarchilab/nLightG.

For manuscripts utilizing custom algorithms or software that are central to the research but not yet described in published literature, software must be made available to editors and reviewers. We strongly encourage code deposition in a community repository (e.g. GitHub). See the Nature Research guidelines for submitting code & software for further information.

Data

DNA and protein sequences for indicators developed in this study were deposited on NCBI (accession numbers ON737776 - ON737782) or are available in Supplementary Data S1. DNA plasmids used for viral production have been deposited both on the UZH Viral Vector Facility (https://vvf.ethz.ch/) and on AddGene. Viral vectors can be obtained either from the Patriarchi laboratory, the UZH Viral Vector Facility, or AddGene. Source data are provided with the manuscript. Raw data can be made available upon reasonable request.

Field-specific reporting

Please select the one below that is the best fit for your research. If you are not sure, read the appropriate sections before making your selection.

☒ Life sciences   ☐ Behavioural & social sciences   ☐ Ecological, evolutionary & environmental sciences

For a reference copy of the document with all sections, see [nature.com/documents/nr-reporting-summary-flat.pdf](#)

Life sciences study design

All studies must disclose on these points even when the disclosure is negative.

Sample size	No sample size calculation was performed. Sample sizes were based on the previous scientific literature in the field (Duffet et al, Nat Methods 2022; Patriarchi et al, Nat Methods 2020; Patriarchi et al, Science 2018).
Data exclusions	During photometry recordings combined with optogenetic stimulation, mice that did not show pupil responses to optogenetic stimulation of the locus coeruleus were excluded from the analysis.
Replication	All experiments were repeated at least three independent times using multiple cell cultures and multiple animal subjects within each group. All replication attempts were successful.
Randomization	Group allocations used in this study were randomly assigned to animals and/or cultured cells.
Blinding	Blinding during group allocations was not adopted in this study and data analysis was performed in an objective and unbiased fashion, as in previous literature (Duffet et al, Nat Methods 2022; Patriarchi et al, Nat Methods 2020).

Reporting for specific materials, systems and methods

We require information from authors about some types of materials, experimental systems and methods used in many studies. Here, indicate whether each material, system or method listed is relevant to your study. If you are not sure if a list item applies to your research, read the appropriate section before selecting a response.

Materials & experimental systems

n/a	Involved in the study
☐	☒ Antibodies
☐	☒ Eukaryotic cell lines
☒	☐ Palaeontology and archaeology
☐	☒ Animals and other organisms
☒	☐ Human research participants
☒	☐ Clinical data
☒	☐ Dual use research of concern

Methods

n/a	Involved in the study
☒	☐ ChIP-seq
☒	☐ Flow cytometry
☒	☐ MRI-based neuroimaging

Antibodies

Antibodies used	chicken anti-GFP (1:750; Thermo Fisher Scientific, cat#A10262). Validated by relative expression by the commercial provider; rabbit anti-TH (1:1000; Merck Milipore, cat#AB152). Routinely validated by Western Blot on PC12 lysates by the commercial provider; Alexa-488-labeled goat anti-chicken (1:1000, Thermo Fisher Scientific, cat#A11039); Alexa-647-labeled goat anti-rabbit (1:1000, Thermo Fisher Scientific, cat#A32733).
Validation	All antibodies were validated by the commercial provider.

Eukaryotic cell lines

Policy information about <u>cell lines</u>

Cell line source(s)	HEK293T cells (ATCC cat#3216)
Authentication	The cell lines were authenticated by the vendor (ATCC) using Short Tandem Repeat (STR) Profiling to detect misidentified, cross-contaminated, or genetically-drifted lines.
Mycoplasma contamination	The cell line used was mycoplasma-free.
Commonly misidentified lines (See <u>ICLAC</u> register)	The study did not involve commonly misidentified cell lines.

Animals and other organisms

Policy information about <u>studies involving animals</u>; <u>ARRIVE guidelines</u> recommended for reporting animal research

Laboratory animals	For ex vivo and in vivo experiments, 6-24 week old mice (mus musculus, C57/Bl6 strain) of both sexes were used. Rat embryos (E17) from timed-pregnant Wistar rats (RccHan:WI, Envigo). Heterozygous B6.Cg-Dbhtm3.2(cre)Pjen/J (DBH-Cre) mice (The Jackson Laboratory) and heterozygous C57BL/6-Tg(Dbh-iCre)1Gsc (DBH-iCre) mice (The Jackson Laboratory) of both sexes were used in this study.
Wild animals	No wild animals were used in this study.
Field-collected samples	No field-collected samples were used in this study.
Ethics oversight	Animal procedures were performed in accordance to the guidelines of the European Community Council Directive or the Animal Welfare Ordinance (TSchV 455.1) of the Swiss Federal Food Safety and Veterinary Office and were approved by the Zürich Cantonal Veterinary Office, the Hamburg state authority for animal welfare and the animal welfare officer of the University Medical Center Hamburg-Eppendorf, National Council on Animal Care of the Italian Ministry of Health.

Note that full information on the approval of the study protocol must also be provided in the manuscript.